2

First Principles Molecular Simulation of Energetic Materials at High Pressures

F. Zhang, S. Alavi, A. Hu, and T.K. Woo

2.1 Introduction

The availability of relatively inexpensive and powerful computing technology has profoundly changed the way in which modern scientific research is conducted in numerous fields. At a rather trivial but highly relevant practical level, the rapid increase in computer power has considerably sped up the pace of theoretical schemes and approaches for simulating bulk material at the atomic level. The results of the simulations have been invaluable in the guidance of experiments and for providing insight into system behavior, particularly under extreme conditions of temperature and pressure. In this respect, a major role has been played by molecular dynamics (MD), which since the pioneering efforts of the 1960s [1, 2] has developed into a mature and active discipline that has been used as a means of simulating and understanding the properties of real systems. More recently, major progress has been achieved in the development of ab initio or "first principles" MD, in which the potential energy and interatomic forces are derived from accurate quantum mechanical electronic structure calculations that are performed as the simulation proceeds [3–5]. This has greatly improved the predictive power of the simulation and opens the way for the reliable simulation of processes in which chemical bonds are formed and broken. The formation and breaking of chemical bonds is simulated with great difficulty in MD based on classical mechanics and empirically derived reactive potentials [6–9].

The development of ab initio MD, along with the rapid development of computer power, has inspired its application to studies of energetic materials and detonation processes. There are several difficult problems currently encountered in the field of molecular condensed matter detonation. Is the initiation of detonation in existing molecular explosives controlled by the thermal decomposition via shock temperature or by initial molecular collisions occurring within the shock front? [6, 10] Could the initial molecular collision and subsequent bond energy release be made the main mechanisms for the initiation and propagation of detonation in a new generation of molecular

explosives, whose detonation velocity could be several times that of current explosives? Would pressure dissociation or momentum-induced decomposition at low temperatures be another possible mechanism for detonation to generate high-speed solid particles products? Experimental support to answer these questions must be derived under extreme conditions of pressure and temperature from observations inside the shock front, thereby requiring measurements on the time scales of 10^{-2}–10^{0} ps. Molecular simulation has offered an alternative avenue towards gaining insights into these challenging problems and guidance to experimental research with energetic materials and detonation processes. High-energy-density materials must feature metastability and a large energy content that mostly originates in transformations of the molecular, atomic and electronic structures. Successful synthesis of these materials and control of the energy release from the structural bonds strongly rely on the understanding of the chemical processes and physics of structural transformations at the atomic level.

In the following we review computations that have recently been carried out in our group on high energy density materials. Quantum mechanics-based, density functional theory (DFT) [11] methods are used to provide atomic-level insight into the physical and chemical properties and processes which occur in these materials. Compared to classical molecular scale simulation methods that are based on empirically derived potentials, the simulations presented here allow for the simulation of complicated covalent bond breaking and formation, such as in the case of molecular decomposition.

The cases discussed include the reaction of nitromethane under binary collision conditions, in the absence and presence of spectator molecules which participate in secondary collisions in the system. Additionally, the reaction of liquid nitromethane under high pressure conditions is studied. Our work on the solid-state phases of covalent nitrogen is also summarized. There are several areas where computations can contribute in these studies. First, direct information about optimized crystallographic lattice parameters and the geometrical parameters of systems can be determined. This can be done for a variety of uncompressed lattices or when external isotropic or anisotropic compression is applied to the crystal. Besides the structural, elastic, and phonon-modes parameters, other important energetic and electronic properties can be evaluated. Among the list of electronic properties some representative examples are the band structure and the total or partial density of states. Furthermore, additional insight can be obtained from population analyses of charge distribution, bond order, and electron and spin density maps.

2.1.1 Introduction to First Principles Molecular Simulation

When studying processes at the molecular level, the most fundamental property of interest is the molecular potential energy surface or simply the potential energy surface (PES). The potential energy surface of a system relates the total energy of a molecular system with the geometric arrangement of

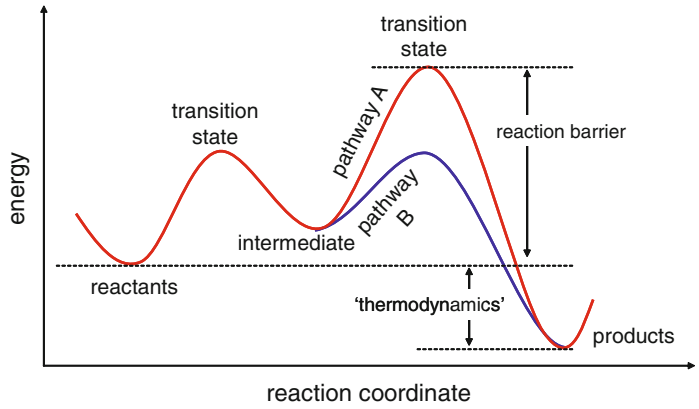

Fig. 2.1. Generic potential energy surface for a chemical reaction. The reaction coordinate represents a combination of nuclear coordinates which links the reactant molecules on the potential energy surface to the products

the atoms that make up the system. Since each atomic nucleus has three spatial degrees of freedom associated (x, y, z in Cartesian coordinate space) the potential energy surface is a 3N dimensional hypersurface where N is the number of atoms that make up the system. A simple one-dimensional potential energy surface of a generic chemical reaction is depicted in Fig. 2.1.

In principle, if the potential energy surface for a given reaction can be calculated, important quantities such as the reaction enthalpy, which is related to the energy content of a material, the reaction barriers, the reaction mechanism, and the structure of a material, among other quantities, can be determined. Thus, a detailed understanding of a reactive process can be achieved via computer modeling of the potential energy surface that in turn provides an avenue for rationally studying reactions and predicting new products at different temperature and high pressure conditions.

A wide array of chemical simulation methods exist and have been used for decades, as outlined in Fig. 2.2. For processes which do not involve the formation or breaking of chemical bonds, the motion of reactants on the potential energy surface can be adequately described by classical potentials. These are also referred to as empirical potentials, molecular mechanics methods, force field methods and ball and spring potentials. For these processes, the inter- and intramolecular forces between the atoms can be described loosely as forces among classical springs (harmonic or anharmonic). The force constants among these "springs" are determined empirically by comparing the predictions of the simulations of thermodynamic properties with experimental results, or higher level ab initio calculations. Thus for processes such as melting, evaporation, and non-reactive shockwaves, classical potentials may be used. Classical potentials have the advantage that they are relatively inexpensive to calculate and, as a result, simulations with thousands to millions of atoms can be

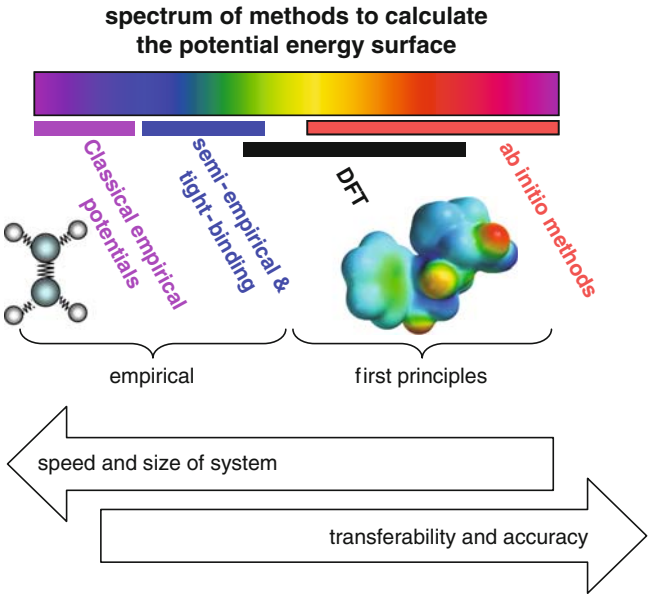

Fig. 2.2. Spectrum of methods to calculate the potential energy surface. Moving toward the left, methods tend to be faster, allowing for more atoms to be simulated. Moving toward the right, methods are more transferable, and often more accurate

performed. The main disadvantages of classical potentials are that they can not be generally used to simulate bond breaking/forming processes, and they are limited in their transferability. The latter caveat means that the empirical constants in the potentials are chosen to reproduce a certain set of properties of a limited given class of materials, and as a result these potentials may be of limited value when simulating materials and properties different from the training set. For simulating processes which involve the formation and breaking of covalent bonds, the use of classical potentials is limited in value, and in these cases, quantum mechanical methods are most often used. We note that there are some 'empirical' potentials that do allow for covalent bond breaking and formation [12–14], but these are still very limited to the class of materials for which the potentials are parameterized.

With quantum mechanical based methods, there is an attempt to solve for the Schrödinger equation or equivalent equations, which provide the electronic structure of the system either in the form of a wave function or electron density. The detailed electronic structure allows one to evaluate the energy of the system, the forces exerted on the nuclear centers, and therefore the all-important potential energy surface. There exists a hierarchy of quantum mechanics methods used in molecular simulation, ranging from fast, empirical methods to more computationally demanding 'first principles' methods. The choice of method to be used in a simulation generally involves striking

a balance between accuracy and computational cost and typically, these two features of a method run contrary to one another. That is, there is usually a high computational price to pay for high accuracy.

In this work, we will restrict ourselves to simulations using 'first principles' quantum mechanical methods. First principles methods sometimes referred to as ab initio methods, use little or no empirical data to construct the electronic structure. As a result, they have a high degree of transferability since they are not constrained by a particular training set. This makes first principles quantum mechanical methods well suited to simulating materials under extreme conditions where available experimental data can be limited or non-existent. The first principles methods of choice for simulating materials and molecules are density functional theory (DFT) methods. DFT strikes a favorable balance between accuracy and computational efficiency that has led to its widespread use in the molecular and material sciences. DFT calculations can routinely be performed on systems containing hundreds or thousands of atoms with modern computers.

2.1.2 Density Functional Theory

The basic premise for DFT is that all ground state properties of a chemical system are uniquely determined by the total electron density rather than the full multielectron wavefunction. This is known as the first Hohenberg–Kohn theorem [15]. This theorem implies that the electronic energy of a molecular system is a functional of the electron density. A functional is simply a function of a function, for example, the value of a variable I has a functional relationship with integrable functions $f(x)$, shown as $I[f]$ for the following case, $I\,[f] = \int_0^\infty f(x)dx$. The value of I depends on the function $f(x)$. In this case, the energy, $\mathrm{E}[\rho]$, is a functional of the electron density, $\rho(\mathbf{r})$, which is in turn a function of the three spatial coordinates ($\mathbf{r}$ or x, y, z in Cartesian space). From the electronic energy of a system, the total energy of the system can be easily determined for a given geometric arrangement of the atoms that make up the system, and, therefore, the potential energy surface can be evaluated. The electronic energy functional is typically divided into components that account for the electron kinetic energy, electron–nuclear interaction potential energy and the electron–electron interaction potential energy:

$$E[\rho] = \underbrace{T[\rho]}_{\substack{\text{kinetic energy}\\ \text{of the electrons}}} + \underbrace{E_{\mathrm{Ne}}[\rho]}_{\substack{\text{nuclear}-\text{electron}\\ \text{interaction energy}}} + \underbrace{E_{\mathrm{ee}}[\rho]}_{\substack{\text{electron}-\text{electron}\\ \text{interaction energy}}}, \tag{2.1}$$

where ρ is the electron density and the square brackets indicate a functional dependence in which the variable ρ is a function of other variables, in this case the spatial coordinates.

In 1965, Kohn and Sham recognized that the utility of (2.1) was severely limited by the lack of a kinetic energy functional, $T[\rho]$ [16]. In fact, previous attempts to use DFT with approximate kinetic energy functionals [17, 18], predicted that chemical bonding should not occur at all [19]. To tackle this situation, Kohn and Sham ingeniously introduced a 'fictitious' non-interacting reference system (analogous to Hartree–Fock orbitals) built from a set of single electron wave functions, or Kohn–Sham orbitals, $\{\psi_i(\mathbf{r})\}$, that sum to give the real electron density ρ,

$$\rho(\mathbf{r}) = \sum_i |\psi_i(\mathbf{r})|^2 \tag{2.2}$$

where the summation index, i, runs over occupied orbitals (loosely one orbital for each electron in the system). The kinetic energy of the non-interacting system can then be calculated as:

$$T_0 = \sum_i \int \psi_i(\mathbf{r}) \left(-\frac{1}{2}\nabla^2\right) \psi_i(\mathbf{r}) d\mathbf{r}, \tag{2.3}$$

Using (2.3) it is possible to rewrite (2.1) as:

$$E[\rho] = T_0 + E_{\mathrm{Ne}}[\rho] + E_{\mathrm{ee}}[\rho]. \tag{2.4}$$

The first term on the right hand side of (2.4) is the kinetic energy of the fictitious electronic system. It should be noted that (2.4) is formally and conceptually different than (2.1). In (2.4), the kinetic energy term, T_0 refers to the kinetic energy of a non-interacting reference system, whereas in (2.1) the kinetic energy term refers to the true interacting system. Using the Born–Oppenheimer approximation, through which all nuclei are treated as fixed point charges, the nuclear–electron term is given by:

$$E_{\mathrm{Ne}}[\rho] = -\sum_{\mathrm{I}} \int \frac{Z_{\mathrm{I}}\rho(\mathbf{r})}{|\mathbf{R}_{\mathrm{I}} - \mathbf{r}|} d\mathbf{r}, \tag{2.5}$$

where the index I runs over all nuclei, Z_{I} is the nuclear charge of atom I, and $\mathbf{R}_{\mathrm{I}}$ are the nuclear coordinates of atom I. This relationship describes the Coulombic attraction between the electrons and the nuclei.

The last term in (2.4), $E_{\mathrm{ee}}[\rho]$, accounts for the interactions between electrons. In Kohn–Sham DFT (KS-DFT), this term is separated into two components:

$$E_{\mathrm{ee}}[\rho] = \frac{1}{2} \int\int \frac{\rho(\mathbf{r})\rho(\mathbf{r}')}{|\mathbf{r} - \mathbf{r}'|} d\mathbf{r}\, d\mathbf{r}' + E_{\mathrm{xc}}[\rho], \tag{2.6}$$

The first term on the right hand side of (2.6) represents the classical Coulombic electronic repulsion of an electron moving in the *average* electric field of the other electrons in the system. The second term, E_{xc}, is the so-called exchange correlation energy, which will be discussed further below.

When (2.5) and (2.6) are inserted into (2.4), one arrives at the following expressing for the electronic energy of the system:

$$E[\rho] = \sum_i \int \psi_i(\mathbf{r}) \left(-\frac{1}{2}\nabla^2\right) \psi_i(\mathbf{r}) d\mathbf{r} - \sum_I \int \frac{Z_I \rho(\mathbf{r})}{|\mathbf{R}_I - \mathbf{r}|} d\mathbf{r} + \frac{1}{2} \iint \frac{\rho(\mathbf{r})\rho(\mathbf{r}')}{|\mathbf{r} - \mathbf{r}'|} d\mathbf{r}\, d\mathbf{r}' + E_{XC}[\rho]. \quad (2.7)$$

This equation forms the basis of Kohn–Sham DFT. In order to solve this equation, one needs to find the Kohn–Sham wave functions Ψ_s that minimize the energy of the system, subject to the constraints that the total number of electrons in the system is conserved and the orbitals used to construct the fictitious electronic system are orthogonal. This involves self-consistently solving a set of one-electron equations. The details of this procedure, although straightforward, are beyond the scope of this discussion and will not be described here; however, the interested reader is directed to Chap. 7 of [11].

The first three terms on the right hand side of (2.7) are well-defined for a given set of orbitals. The accuracy of KS–DFT is thus dependent upon the expression for the last term, E_{xc}, which serves as a depository for contributions to the electronic energy that are not adequately described by the other terms in (2.7). These energy contributions include those arising from the correlated motion of electrons due to instantaneous electron–electron interactions (correlation), the correlated motion of electrons due to the Pauli exclusion principle (exchange), a correction for the difference between the kinetic energy of the fictitious electronic system of non-interacting orbitals and that of the true system, and a correction for the interaction of the electron with itself. The specific details of these energy contributions will not be considered in greater detail here.

The exchange-correlation energy, E_{xc}, is evaluated with the use of a functional, which is called the exchange-correlation (XC) functional. The form of this functional is unknown; however, if it was determined exactly, (2.7) would provide the exact ground state energy for the system. Although the true XC functional remains unknown, numerous attempts have been made to develop approximate XC functionals (e.g., see Chap. 6 of reference [11]). In general, approximate XC functionals are developed through either a consideration of the fundamental physics pertaining to electron–electron interactions or fitting parameters in various functional forms to experimental data. Although the former approach is more elegant, the latter often produces functionals that are very accurate for chemical applications.

The simplest XC functionals are based solely upon the value of the electron density [20,21]. This approach is termed the local density approximation (LDA) and is generally too inaccurate for use in most chemical applications. Significant improvements in accuracy are achieved if the XC functional depends on the value and gradient of the electron density [22]. This is termed the generalized gradient approximation (GGA). GGA XC functionals are used

commonly in many chemical applications. More sophisticated functionals can be obtained by incorporating higher-order derivatives of the electron density and other quantities. However, for simulations of liquids and solids, GGA XC functionals are used in the vast majority of DFT calculations.

As noted above, DFT is currently the most popular method for routine quantum mechanical calculations. This popularity, which surged in the early 1990s, is due to the development of accurate XC functionals. These functionals offer accuracy which rivals that of high-level wave function-based methods. In terms of cost, DFT calculations can be performed on systems containing up to a few thousand atoms with modern computers. In terms of accuracy, studies [23, 24] show that LDA, BP86 [25, 26] (GGA), PBE [27] (GGA) and B3LYP [28, 29] functionals yield mean absolute errors of 36.4, 10.3, 8.6 and 2.2 kcal mol^{-1}, respectively, for the atomization energies of the molecules in the G-2 set, [30] which is a standard benchmark database for the assessment of the accuracy of theoretical methods. Calculations of reaction barriers for a set of 76 reactions showed that LDA, BP86 [25]; (GGA), PBE [27] (GGA) and B3LYP [26, 29] (hybrid) DFT functionals yielded errors of 14.9, 8.8, 8.7 and 4.3 kcal mol^{-1} with respect to the results of high-level calculations [31].

2.1.3 Plane Wave Basis Sets

In most practical DFT calculations the Kohn–Sham single electron orbitals, ψ_i., are expressed as a linear combination of basis functions, χ:

$$\psi_i(\mathbf{r}) = \sum_{\nu=1}^{K} c_{\nu i}\chi_\nu(\mathbf{r}), \tag{2.8}$$

where ν is the index of the basis function, K is the total number of basis functions and $c_{\nu i}$ is the mixing coefficient of basis function χ_ν, which determines the contribution of basis function χ_ν to orbital ψ_i. When optimizing the wave function, the coefficients $c_{\nu i}$ are variables that are altered to yield the 'best' wave function for the system, while the basis functions themselves are unaltered. The details of the procedure used to optimize these coefficients will not be discussed here; however, the interested reader is directed to Chap. 3 of [32] or Chap. 7 of [11]. Although any type of mathematical function can be used as a basis function, two types of basis functions have achieved great popularity: localized, atom-centered functions and delocalized plane waves. Localized, atom-centered basis functions are based on the notion that a molecular system is built up from atoms, and hence the total electronic wave function can be represented as a combination of atomic orbital-like functions, which are centered on specific nuclei. Atom-centered basis functions have achieved widespread use in the quantum chemistry community, where so-called Gaussian functions [33] are the most common type of basis function. For the work presented in this chapter, localized basis functions are used sparingly, and will not be discuss in further detail.

An alternative to atom-centered, localized basis functions involves the use of delocalized functions, which are not associated with specific nuclei. The use of such functions is inspired by the notion that electrons in periodic systems are only slightly perturbed by the presence of nuclei, and hence the electronic wave functions should most closely resemble those of free electrons. This description is particularly suited to periodic, conducting systems such as metals. With such systems in mind, one defines a periodic simulation cell (vide infra), e.g., a unit cell for a crystalline material, and calculates the electronic wave function within this cell. The natural basis set for such a calculation is a set of plane waves [34]:

$$\chi_{\mathrm{PW}}(\mathbf{r}) = \frac{1}{\sqrt{\Omega}} e^{i\mathbf{G}\cdot\mathbf{r}}, \tag{2.9}$$

where Ω is the volume of the simulation cell and $\mathbf{G}$ is given by the reciprocal lattice vectors of the cell. A plane wave basis set includes all plane waves up to some maximum value of $\mathbf{G}$.

Plane wave basis sets have several advantages over atom-centered basis functions. First of all, a plane wave basis set allows one to move between real and reciprocal spaces through the use of Fast Fourier Transforms. This allows one to calculate quantities in the most convenient space. For example, derivatives in real space are simply multiplications in reciprocal space, and hence it is convenient to perform such calculations in reciprocal space. The fact that plane waves are not associated with specific nuclei also simplifies certain types of calculations. Along the same lines, plane waves treat all regions of space equally, and hence a plane wave basis set is complete, which eliminates basis set superposition errors that occur when using atom-centered basis functions. Finally, plane waves are suited to calculations of periodic systems, which will be discussed ahead.

A significant drawback of plane wave basis sets is that a huge number of plane waves must be used to accurately describe the localized wavefunctions in regions around the nuclei. Specifically, the wavefunction and electron density vary rapidly as one approaches a nucleus. Accurately describing these rapid changes requires using a plane wave expansion up to very high values of $\mathbf{G}$, and hence a large number of plane wave basis functions must be considered in the calculation. In practice, tens or hundreds of thousands of plane wave basis functions must be used to achieve the same level of accuracy that can be attained with a few hundred Gaussian basis functions.

The accuracy and size of the plane wave basis set is determined by the highest value of $\mathbf{G}$ considered in the plane wave expansion. This is determined by taking advantage of the relationship between $\mathbf{G}$ and the kinetic energy of the plane wave:

$$E_{kin}(\mathbf{G}) = \frac{1}{2}|\mathbf{G}|^2, \tag{2.10}$$

which allows one to define a parameter E_{cut} that corresponds to the kinetic energy of the plane wave with the highest value of $\mathbf{G}$ in the basis set. The parameter E_{cut} is termed the kinetic energy cutoff. Assigning a value for

E_{cut} indicates that all plane waves where $\frac{1}{2}|\mathbf{G}|^2 \leq E_{cut}$ are included in the plane wave basis set. Without going into details, this leads to the following expression for the number of plane waves in the basis set:

$$N_{\text{PW}} \approx \frac{1}{2\pi^2}\Omega E_{\text{cut}}^{3/2}. \tag{2.11}$$

Equation (2.11) indicates that the number of plane waves considered in the calculation increases with both the volume of the simulation cell, Ω, and E_{cut}.

Thus in summary, plane waves are an alternative to atom-centered, localized basis sets. Plane waves are particularly suited to periodic systems and their use simplifies certain aspects of quantum chemical calculations through the flexibility offered by a dual space representation and the completeness of the basis set. The major drawback of plane waves is that a huge number of basis functions must be used to attain a level of accuracy that is comparable to that achieved with even a small number of localized basis functions.

A final point that is closely related to basis functions involves the use of pseudopotentials (also known as effective core potentials) to replace the core orbitals and to smooth the valence orbitals near the nuclei. For example, in carbon, which has a $1s^2 2s^2 2p^2$ electronic configuration, the 2s and 2p electrons would be treated with a basis set, while the 1s electrons would be represented by a pseudopotential. The motivation for eliminating the explicit treatment of core electrons stems from the notion that these electrons do not contribute significantly to chemical bonding, and hence the core states are altered minimally during chemical reactions. As such, the core states do not need to be treated explicitly in most quantum mechanical calculations. This dramatically decreases the number of basis functions needed for a particular calculation, which decreases computational cost. An additional advantage of pseudopotentials is that relativistic effects associated with core electrons in heavy atoms can easily be incorporated into the calculation without additional computational effort. In practice, all plane wave calculations use pseudopotentials to represent the core states of all atoms.

2.1.4 Periodic Boundary Conditions

It is often of interest to perform simulations of bulk liquids or bulk solids. By definition, such systems extend across length scales that are inaccessible through quantum mechanical (or even classical) simulation. One means of simulating these systems is to perform a calculation on a small system that is representative of the bulk material and repeat this small system infinitely in all three spatial directions. A two-dimensional example is shown in Fig. 2.3, where the central cell is repeated in the plane of the page. Representing a system in this manner is termed using periodic boundary conditions (PBCs). In what follows, a few key points regarding the use of PBCs in quantum mechanical calculations are qualitatively described.

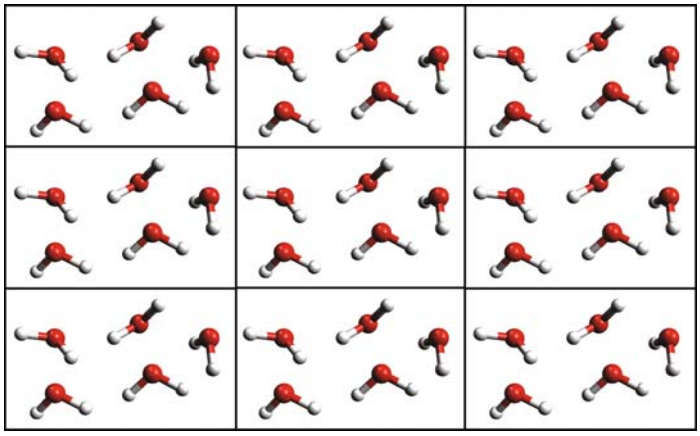

Fig. 2.3. Periodic boundary conditions in two dimensions. The central cell contains five water molecules and is repeated exactly in both spatial directions that define the plane of the page. Nine cells are shown explicitly; however, the system should be repeated infinitely in all directions

As mentioned above, the use of PBCs involves defining a simulation cell and repeating this cell periodically to form an infinite crystal. In this scheme, quantities such as the wave function are periodic and must be continuous across the walls of neighboring simulation cells. This introduces constraints into the calculations which ensure that the central simulation cell interacts with its periodic images, although the calculation is only performed on the central simulation cell. Long range electrostatic interactions between the periodic images, can be accounted for by using techniques such as Ewald summations [35]. This property of PBCs proves useful when simulating bulk materials, where any given atom should interact with those throughout the material. For example, in a crystal, which is composed of periodically repeated unit cells, the atoms in a given unit cell should interact with those in the other unit cells. In the case of non-crystalline systems, e.g., liquids or amorphous solids, it is desirable to study bulk systems; however, such systems should not be periodic. PBCs can still be used to approximate these systems by defining a large "central" simulation cell, which minimizes the effect of externally imposed periodicity on the behavior of the system. It should be noted that imposing PBC implies some constraints on the long-range structure and correlations in bulk systems. These must be carefully considered when simulating long-range properties such as low-frequency phonon modes.

2.1.5 Molecular Dynamics

In the preceding section, we have outlined how first principles density functional theory calculations can be used to calculate the potential energy surface. Exploring the PES is important because it provides insight into chemical

processes that may occur. Conventional studies of materials and molecules that apply first principles quantum mechanical methods often do so in a static sense. That is, the behavior on the PES is considered in the zero Kelvin limit and then extrapolated to finite temperatures. Furthermore, static calculations focus on particular regions of the PES corresponding to relevant species such as the presumed reactants, products and transition state associated with a given processes. 'Static' calculations are extremely powerful and widely used. In this chapter, more novel ab initio molecular dynamics (MD) simulations are also presented. These ab initio MD simulations allow one to observe the evolution of a system in space and time at the molecular level subject to a given set of macroscopic external conditions, e.g., temperature and pressure. It is noted that MD simulations provide a great deal of qualitative insight into chemical processes, yet can also be applied quantitatively. In what follows, we discuss the MD methodology and its use in the study of chemical reactions.

Most MD calculations treat the nuclei comprising a chemical system as classical particles whose trajectories can be determined with Newtonian equations of motion:

$$\mathbf{F}_i = m_i \mathbf{a}_i = m_i \frac{d^2 \mathbf{R}_i}{dt^2} \tag{2.12}$$

where the force on atom i, $\mathbf{F}_i$, is obtained by differentiating the potential energy with respect to the nuclear coordinates:

$$\mathbf{F}_i = -\frac{\partial E(\mathbf{R})}{\partial \mathbf{R}_i}. \tag{2.13}$$

Unfortunately, it is not possible to analytically integrate (2.12) for a many-body system, and one must numerically integrate the system of coupled differential equations representing the trajectory over a series of small time steps. The general procedure is as follows. At a certain time, t, the nuclei are described by a set of positions and momenta, $\mathbf{R}_i(0)$ and $m_i \mathbf{V}_i(0)$. The potential energy for the system is calculated and used to determine the forces on the nuclei, which are then used to update the nuclear positions and momenta to their values at a later time, $t + \Delta t$. The process is then repeated until a sufficiently long total period of time is simulated. The time intervals, Δt, used in this process must be short enough to capture the highest frequency motions in the system, which typically correspond to bond vibrations. As such, these intervals are on the order of 10^{-15} s, and hence $\sim 10^6$ force calculations must be performed to simulate one nanosecond of time. Despite the considerable computational expense associated with this procedure, MD simulation has been an exceedingly powerful and popular tool for over 50 years [36–38].

An important feature of MD simulations is the ability to study reactions under a given set of conditions. For instance, by properly scaling the nuclear kinetic energies it is possible perform simulations at a given temperature. Means of applying pressure to the system also exist. In a constant volume simulation with PBC, a simulation with high molecular densities will effectively

lead to high simulation pressures. Alternatively, pressure and temperature can be added as independent dynamic variables in the equations of motion that are coupled to the positions and momenta of the molecules in the simulation [35]. These capabilities are quite important when studying the influence of external conditions on a reaction. By comparison, temperature and pressure can only be incorporated into static calculations in an *ad hoc* manner.

2.1.6 Ab initio Molecular Dynamics

In the preceding subsection, the classical MD methodology was briefly introduced in a generic sense, with the PES considered merely as a means of obtaining the forces on the nuclei. For the vast majority of MD simulations, the PES is evaluated with classical potentials, which are parameterized functions that subdivide the potential energy into distinct contributions associated with bond lengths, angles, dihedrals, electrostatics, etc. With the exception of a few specific cases, classical potentials cannot accurately describe changes in bonding, and hence are not suitable for use in the simulation of chemical reactions, i.e., bond formation and dissociation. In order to study such processes, it is necessary to explicitly consider the electronic structure of the system. A popular way to do this is ab initio molecular dynamics (AIMD) [39].

In the AIMD approach, the potential energy in (2.13) is derived from a QM calculation; typically at the density functional level of theory. The explicit consideration of the electronic structure of the system in this manner leads to a powerful simulation method that is capable of describing chemical reactions. In fact, because the system moves on the electronic PES according to well-defined equations of motion, i.e., Newton's equations, one can, in principle, simply initiate an AIMD simulation, follow the motion of the system and observe chemical reactions without having any preconceived notions of what the potential energy surface describing those reactions may be. The ability of AIMD simulations to investigate known reactions and identify new reactions has led to a dramatic increase in the popularity of this method in recent years.

AIMD simulation is not without its drawbacks, as these calculations suffer from many limitations due to the computational expense of the first principles QM calculations. If the potential energy is derived from a DFT calculation, it is typically only possible to perform simulations on systems composed of a few hundred atoms, and only sub-nanosecond time scales may be considered. Despite these limitations, AIMD simulation has recently experienced a tremendous increase in popularity and is commonly applied to a wide variety of systems [4, 5, 40–42].

Two popular types of AIMD simulations exist. The first approach is called Born–Oppenheimer AIMD (BO-AIMD) and involves optimizing the electronic structure of the system at each time step of the simulation. That is, a full wave function optimization is performed at each time step, and the resulting potential energy is used to determine the forces on the nuclei. BO-AIMD is

an intuitive approach to AIMD simulation, yet is computationally expensive because of the tremendous number of wave function optimizations that must be performed.

The second main type of AIMD simulation is known as Car–Parrinello AIMD (CP-AIMD) [3] and involves treating the electronic states as effective dynamic variables which are propagated according to the classical Newtonian equations of motion. In a CP-AIMD calculation, the first-principles method used is almost exclusively DFT, where the Kohn–Sham orbitals are optimized at the very first step of the simulation only. Then, they are assigned a fictitious mass, μ, and propagated in time according to classical equations of motion through the following extended Lagrangian:

$$\mathcal{L}_{CP} = \underbrace{\frac{1}{2}\sum_{I=1}^{N_{atoms}} M_I \dot{\mathbf{R}}_I^2}_{\substack{\text{nuclear kinetic}\\ \text{energy}}} + \underbrace{\frac{1}{2}\sum_{i=1}^{n_{orbitals}} \mu_i \left\langle \dot{\psi}_i \,\middle|\, \dot{\psi}_i \right\rangle}_{\substack{\text{orbital kinetic}\\ \text{energy}}} - \underbrace{E^{DFT}[\rho]}_{\substack{\text{electronic}\\ \text{potential}\\ \text{energy}}} + \underbrace{\sum_{i,j} \Lambda_{ij} \left(\langle \psi_i \mid \psi_j \rangle - \delta_{ij} \right)}_{\text{orthonormality constraints}} . \tag{2.14}$$

The first term of (2.14) is the classical kinetic energy of nuclei with masses $\mathrm{M_I}$, the second term is the fictitious 'classical' kinetic energy of orbitals due to the electronic degrees of freedom with inertial parameters (fictitious masses) μ_i, the third term is the electronic energy as described in (2.7), and the last term is the constraints to maintain orthogonality of orbitals. Upon substitution of (2.14) into Lagrange's equation of motion one obtains the Car–Parrinello equation of motion for both the nuclei and the KS orbitals:

$$M_I \ddot{\boldsymbol{R}}_I = -\frac{\partial E(\psi_i, \boldsymbol{R}_I)}{\partial \boldsymbol{R}_I} \tag{2.15}$$

$$\mu_i \ddot{\psi}_i = -\frac{\partial E(\psi_i, \boldsymbol{R}_I)}{\partial \psi_i} + \textit{orthogonolity constraints}. \tag{2.16}$$

In this approach, the Kohn–Sham orbitals are propagated as classical degrees of freedom at the same time the nuclear motion is treated. Therefore, there is no need to optimize the electronic structure at each time step as in the BO-AIMD approach. It is important to note that although the orbitals are treated as classical degrees of freedom, the electronic structure is still determined quantum mechanically. It is also noted that the mass, μ, is a fictitious quantity assigned to the orbitals that should not be confused with the mass of the electron. Moreover, in the limit that μ approaches zero, the Car–Parrinello equation converges to the KS equation so that E is minimized and the Born–Oppenheimer limit is recovered.

The key to successfully performing a CP-AIMD simulation lies in preventing the transfer of energy between the nuclear and electronic subsystems. This

is achieved by altering the value of μ such that the power spectra of these two subsystems do not overlap, i.e., μ should be kept small to ensure that the orbitals oscillate at frequencies much higher than those of the nuclei. Furthermore, using a small value for μ allows the orbitals to adjust quickly to changes in the nuclear configuration, which keeps the system close to the ground state PES. In a properly performed CP-AIMD simulation the electronic structure will remain close to the true PES, and hence the dynamics observed in a CP-AIMD simulation closely follow those which would be determined in a BO-AIMD calculation.

As indicated above, the main advantage of the CP-AIMD approach is that the electronic structure is only optimized once during the course of a simulation. This can significantly decrease computational cost compared with a BO-AIMD simulation, where the electronic structure is optimized at each time step. However, properly integrating the orbital dynamics, which oscillate at high frequencies, requires the use of times steps, Δt, that are typically an order of magnitude smaller than those used in a BO-AIMD simulation. This decreases the computational advantage of CP-AIMD simulations over BO-AIMD simulations. Nonetheless, the former is faster in most cases and has become the most popular AIMD simulation technique for studying chemical systems.

2.2 Collision Dissociation of Nitromethane

Although numerous theoretical reports focusing on nitromethane (NM) have appeared in the literature [43–50] the decomposition mechanism of liquid NM under shock conditions remains elusive. The C—N bond is the weakest bond in NM and therefore unimolecular C—N bond scission has often been implicated as the dominant decomposition pathway. However, a number of high pressure studies do not support this mechanism, [51,52] vide infra. To gain some insight into these decomposition pathways bimolecular collision MD simulations have been performed by a number of researchers [53,54]. A summary [54] of bimolecular collisions of NM in a variety of orientations and a large range of incident collision velocities is shown in Table 2.1. For the offset anti-parallel molecular orientation, the critical velocity for successful dissociation was found to be $7.0\,\mathrm{km\ s^{-1}}$, higher than the average atomic velocities expected at the shock front of a detonation [55]. Although these bimolecular collision simulations provide a qualitative glimpse into the shock-induced dissociation process, they cannot account for the effects that neighboring molecules may have on the dissociation mechanism. This issue is addressed in first principles Car–Parrinello molecular dynamics (CPMD) simulations of multimolecular collisions of NM.

2.2.1 Impact of a Single Molecule on Multiple Molecules

The previous bimolecular collision simulations are limited to collision-induced reactions without neighboring confinement and collision sequences beyond

Table 2.1. Threshold collision velocities (km s^{-1}) determined from multimolecular and bimolecular collision simulations

Orientation		Threshold collision velocity	
		Multimolecular	Bimolecular
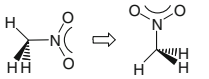	Perpendicular	12.0	8.0
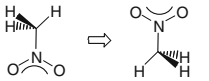	Anti-parallel	11.0	10.5
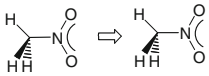	Head-to-tail	11.0	8.5
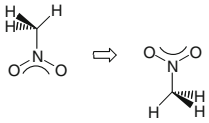	Offset Anti-parallel	12.0	7.0

the initial impact are meaningless due to only the two isolated molecules involved. Multimolecular collision simulations offer a substantial improvement since they allow for possible collision-induced reactions involving neighboring molecules beyond the initial impact. The effects of multiple collisions on the decomposition mechanism are important in that they determine whether the molecular decomposition occurs at the initial shock wave front or after further thermalization of the shock wave energy. This issue can have important implications on the behavior of the material as a high energy density material. Due to the very short time scales involved in passing of the initial shock wave and thermalization stages, information regarding the decomposition mechanism at these time scales can be experimentally difficult to obtain. This makes the use of simulation methods very useful for the study of this phenomenon.

The first study of multimolecular collisions involves collisions by the impact of a single molecule on multiple molecules. The simulations are conducted under the same four collision orientations of the initial colliding NM pair of molecules as the bimolecular collisions reported in Table 2.1. A total of 13 NM molecules are placed in an orthorhombic simulation cell of $19.0 \times 14.2 \times 14.2$ $Å^3$ such that one molecule is placed at one end of the simulation cell and the remaining 12 molecules are placed at the opposite end. The simulations are initiated by propelling the separated molecule into a stationary molecule, embedded in the cluster of NM molecules as illustrated in Fig. 2.4. The cluster of 12 molecules is randomly oriented and possesses a density of 1.14 g cm^{-3}, corresponding to the density of liquid NM at ambient pressure and temperature. The incident collision velocities range from 6 to 12 km s^{-1} for various orientations of the two colliding molecules. Each multimolecular collision simulation is run for 3,500 time steps or 0.507 ps.

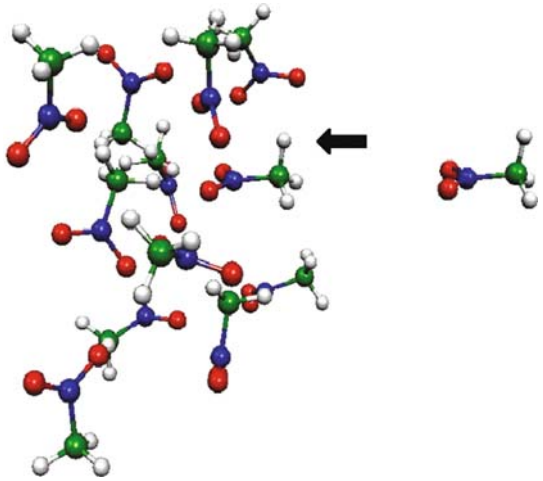

Fig. 2.4. Schematic of the single-molecule on multi-molecule nitromethane collision simulation with the head-to-tail orientation for the initially colliding pair

As evident from Table 2.1, the threshold collision velocities determined from the multimolecular collision simulations are significantly higher than those found previously from bimolecular collision simulations for each molecular orientation investigated. In all cases of multimolecular collisions, the sub-critical velocity collisions induce initial C—N bond scission of the incoming and stationary molecules. However, the neighboring molecules act as a trap to confine the CH_3 and NO_2 fragments produced, thereby enabling them to recombine to form intact NM molecules. The C—N bond then alternately breaks and reforms as the simulation continues until finally it remains intact when there is insufficient energy to break it. At the threshold collision velocities, the recoiling fragments produced during the initial collision possess enough translational energy to overcome the confinement forces of the neighboring molecules leading to permanent cleavage of the C—N bond to yield CH_3 and NO_2. Collisions of more than two molecules are observed, for instance, for the perpendicular molecular orientation at 12 km s^{-1}, where collisions occur between four NM molecules including the incoming, the stationary and two neighboring molecules. This results in permanent C—N bond cleavage of the stationary molecule, while the other molecules involved recombine to form intact NM molecules. Permanent C—N bond scission is observed in both the incoming and stationary NM molecules in the offset anti-parallel orientation at its threshold velocity of 12 km s^{-1}, while the anti-parallel and head-to-tail orientations display permanent C—N bond cleavage of the incoming NM molecule at the threshold velocity of 11 km s^{-1}. These velocities are not available under conventional detonation conditions of nitromethane with a shock velocity of 6–7 km s^{-1} where the molecular collision velocities are even less than this value.

While the threshold velocity of multimolecular collisions is higher than that of bimolecular collisions in all the collision orientations, the predominant mechanism of decomposition remains the C—N bond cleavage as in the bimolecular collisions. A different fragmentation mechanism, initial C—H bond scission of the stationary molecule is observed in one of the high velocity multimolecular collision simulations (12 km s^{-1} in a head-to-tail orientation). The initial C—H bond cleavage is followed immediately by the migration of this free H atom to one of the O atoms of the incoming NM molecule which induces N—O bond cleavage of this NM molecule yielding OH and CH_3NO. The N—O bond of the stationary molecule is then cleaved and the free O atom migrated to the CH_2 group of the stationary molecule, thereby inducing C—N bond cleavage to yield CH_2O and NO fragments. The final products produced from this cascade of reactions are: OH, CH_2O, NO, and CH_3NO.

2.2.2 Impact of Multiple Molecules on Multiple Molecules

The multimolecular collision simulations are further extended to the collisions between two groups of molecules as depicted in Fig. 2.5. The chemical system of 32 NM molecules is contained in a cubic simulation cell 14.2 Å on each side. The density of the 32 molecules in the cube corresponds to 1.14 g cm^{-3} for liquid NM. Periodic boundary conditions are employed to better represent the bulk material properties and effects of neighboring molecules. In an identical setup without using periodic boundary conditions, molecules leaving the cell will effectively be in a vacuum and eventually disperse as a result of Brownian motion. Initial positions for the simulation were first obtained from a classical MD simulation. The initial orientations and velocities of each of the NM molecules in the simulation cell are derived from an AIMD of a sample that was equilibrated for approximately 4.36 ps at 298.15 K with a Nose–Hoover thermostat. Eight NM molecules, occupying the most right-hand quarter of the simulation cell, are translated linearly forward to impact into the other 24 NM molecules occupying the rest of the cell as shown in Fig. 2.5. In each simulation, all eight NM molecules are assigned a uniform initial velocity ranging from 2 to 10 km s^{-1}.

The simulations are further characterized as *static* or *dynamic* simulations. The static simulations are similar to the previous simulations of bimolecular collisions and single-to-multiple molecular collisions, in which the kinetic energy and temperature of the molecules are initially set to zero. The eight molecules occupying the right-hand quarter of the cube are then translated forward with their assigned velocity. In the dynamic simulations, all 32 molecules initially possess equilibrium velocity and the total kinetic energy corresponds to the kinetic energy of the equilibrated sample of liquid NM at 298.15 K and 1 atm. The eight molecules occupying the right-hand quarter of the simulation cube are translated with an assigned velocity in addition to their equilibrium velocity. Thus, the dynamic simulations are considered more realistic than the static simulations. All simulations were performed for 5,000 time steps or 0.725 ps.

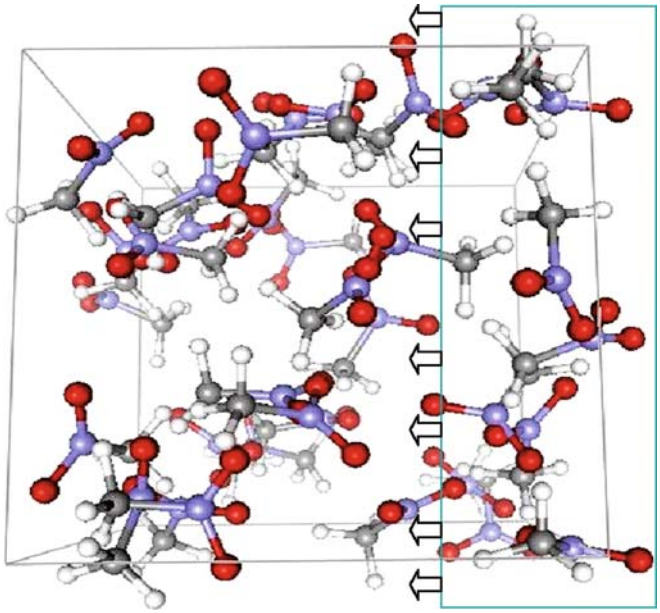

Fig. 2.5. Schematic of the multiple-molecule on multiple-molecule collision simulations

Figure 2.6 shows the dynamic simulation results for average C—N bond lengths of all 32 NM molecules as a function of time at collision velocities ranging from 2 to 10 km s^{-1}. At lower velocities, the bond lengths oscillate around the initial bond lengths. The initial bond length at 25°C is slightly higher than its ideal bond length, which is defined for 0 K in the gas phase and imparts the lowest total energy to the molecule. The ideal bond lengths for the C—N, N—O and C—H are 1.46, 1.22 and 1.10 Å, derived from geometry optimizations of the isolated nitromethane molecule at the PBE/6-31G(d,p) level. A bond is considered dissociated if the distance between the atoms of the bond is greater than 1.5 times the ideal bond length which corresponds to 2.19 Å for the C—N bond. No bond breakage was observed at velocities of 2–6 km s^{-1}. However, for a collision velocity of 8 km s^{-1}, there is a slight increase in the average C—N bond distance in the simulations approximately 500 time steps into the simulation, which further increases at around 1,250 time steps. Qualitative examination of the simulation reveals that the C—N bond of a single nitromethane molecule dissociated at approximately 1,250 time steps. However, the neighboring molecules confine the CH_3 and NO_2 fragments produced, thereby enabling them to recombine to form an intact NM molecule at nearly 1,600 time steps. The C—N bond then alternately breaks and reforms as the simulation continues until finally it remains intact when there is insufficient kinetic energy to overcome the bond strength and the confinement forces of neighboring molecules. At 8 km s^{-1}, while the average

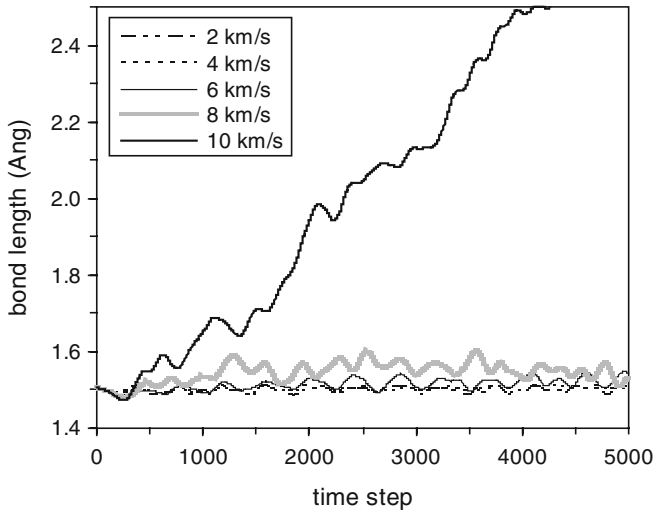

Fig. 2.6. Average C—N bond length as a function of time at 2–10 km s^{-1} velocity of impact of multiple molecules on multiple molecules. The initial temperature and pressure of the molecules in the simulation are 25°C and 1 atm

N—O and C—H bond lengths oscillate around their initial bond lengths at enlarged fluctuation amplitude, no N—O and C—H bonds are broken.

As the collision velocity is increased to 10 km s^{-1} the first C—N bond breakage is observed at 610 time steps, resulting in an increase in average bond length to 1.6 Å (Fig. 2.6). The time delay from the initial impact is ∼0.05 ps, which is shorter than the time delay at the collision velocity of 8 km s^{-1} (∼0.13 ps). The time delay between the initial impact and the C—N bond breakage and its dependence on impact velocity are likely associated with the conversion of translational energy to vibrational energy required for cleavage of the bond. As time proceeds, more and more C—N bonds are permanently broken as shown in Fig. 2.7. Breakage of the N—O and C—H bonds occurs only at 10 km s^{-1} and in a much delayed time. Nearly 2,600 time steps elapse till the first N—O bond dissociation and 3,000 time steps elapse till the first C—H bond dissociation. In all cases of N—O bond dissociation, bond cleavage occurs on an intact NM molecule and results in migration of the oxygen atom to a methyl fragment forming a formaldehyde intermediate. Also, the interaction of two methyl fragments repeatedly forms and breaks short-lived ethane. The C—H bond cleavage results in only a small number of hydrogen atoms that migrate back and forth to the nitro group of neighboring nitromethane.

The fact of the earlier C—N bond cleavage suggests that the predominant mechanism of decomposition remains the C—N bond breakage into the nitro and methyl groups at the threshold collision velocity between 8 and 10 km s^{-1}. As indicated in Table 2.1, this threshold velocity is less than the

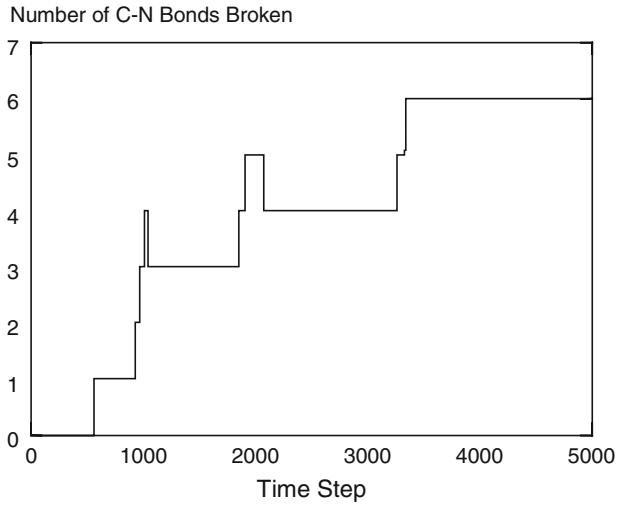

Fig. 2.7. Number of C—N bonds broken as a function of time at 10 km s^{-1} velocity of impact of multiple molecules on multiple molecules. The initial temperature and pressure of the molecules in the simulations are 25°C and 1 atm

values obtained from the collisions of a single molecule on multiple molecules. This is so because in the collisions of multiple molecules on multiple molecules, the total impact kinetic energy received by the receptor molecules is larger and the latent neighboring confinement becomes weaker due to the distributed impact kinetic energy.

The static simulations provide an identical decomposition mechanism and threshold collision velocity based on the C—N bond cleavage. The difference between the static and dynamic simulations lies in the time delay of the decomposition and the rate of bond length increase that becomes apparent at the impact velocity of 10 km s^{-1} as shown in Fig. 2.6. The difference observed can be explained by the additional kinetic energy at room temperature and pressure available in the dynamic simulations. This additional energy manifests itself vibrationally and promotes decomposition once initial bond breakage begins.

It is clear from these simulations that a strong shock can result in rapid decomposition of nitromethane, in times far short for thermal equilibrium to have been established. The simulations of this section indicate that the initial velocities required for the direct decomposition of nitromethane molecules is in the range of 8–10 km s^{-1}. Experimentally, it was found that the average speed of nitromethane molecules at the detonation shock front is about 2.5 km s^{-1} [56]. This shows that the nitromethane decomposition reaction mainly occurs in the thermalization stage behind the shock front of a conventional detonation. This conclusion also appears to be confirmed by recent experiments of the incident or multiple reflected shock compression initiation

of detonation in liquid nitromethane, where the temperatures for incident and multiple reflected initiation upon shock compression are equal to about 700 K, while the multiple reflected shock pressure reaches 8 GPa, nearly two times that of the incident shock [57, 58]. The 8–10 km s^{-1} decomposition threshold collision velocity further suggests that the collision-induced detonation initiation in the shock front would likely be dominant for a detonation velocity beyond 15–20 km s^{-1} in a molecular condensed matter. This would result in a megabar detonation pressure since the detonation pressure is approximately proportional to the square of the detonation velocity. In order to examine the threshold pressure for mechanical dissociation under minimal thermal influence, first principles molecular dynamics simulations of static compression at low temperatures will be discussed in the next section.

2.3 Pressure Dissociation of Nitromethane

The reactions of high energy density materials under low temperature – high pressure conditions are of interest. For this purpose, the high pressure decomposition of nitromethane has been studied. To study the effects of isotropic pressure on the decomposition of NM, Car–Parrinello ab initio MD simulations were performed. Periodic boundary conditions were utilized with a simple cubic simulation cell and 32 nitromethane molecules such that the experimentally measured bulk density of 1.139 g cm^{-3} at 298 K and 1 atm pressure was reproduced. This simulation cell volume was then shrunk by a factor of 1.5–3.0. Well equilibrated classical MD simulations were used as the starting point.

Initial geometric configurations for the ab initio MD simulations were extracted from well equilibrated classical MD simulations. The cell volume was compressed isotropically by a factor of up to 3. Slow heat up was performed (50 K $\rightarrow$ 150 K $\rightarrow$ 300 K). At 300 K, equilibration was performed for 25,000 time steps (ca. 3.5 ps) and production runs were performed for 25,000 time steps. The R_{CN}, R_{NO}, and R_{CH} bond lengths at different compressions are shown in Fig. 2.8.

The ab initio MD simulations of compressed liquid NM show no molecular decomposition at compression factors of 2.0 and 2.5 at 300 K. However, when the liquid is compressed by a factor of 3.0 an interesting pressure-induced molecular decomposition is observed at 150 K after equilibration for about 3,300 time steps. An intermolecular H atom transfer event occurs between two very closely spaced molecules aligned in an anti-parallel alignment, as illustrated in the MD trajectory snapshots shown in Fig. 2.9. As illustrated in Fig. 2.9, the CH_3 group of one of the NM molecule re-orients itself such that two of its H atoms lie in the same plane as the NO_2 fragment and the other H atom is oriented nearly perpendicular to this plane directed at the O atom of the adjacent NM molecule. This H atom then transfers from the C atom of the first NM molecule to the O atom of the second NM molecule to yield the

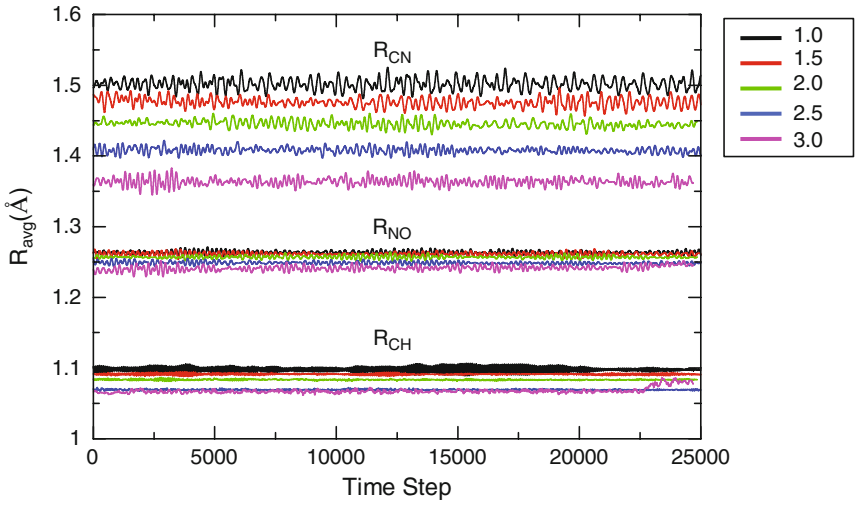

Fig. 2.8. Changes in intramolecular bond distances with pressure at 300 K. The colors correspond to different compression factors (effective pressures) of the simulation

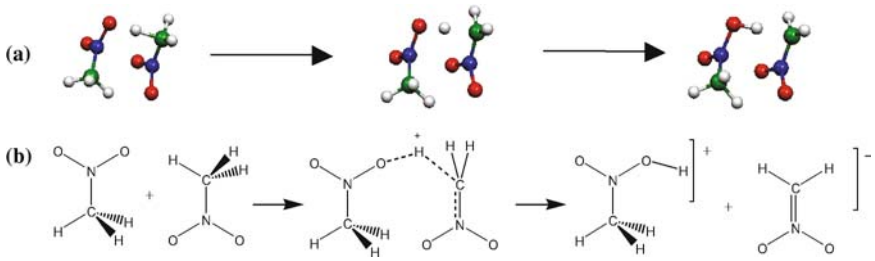

Fig. 2.9. (**a**) snapshots from ab initio MD simulation of highly compressed liquid nitromethane showing a proton transfer event. (**b**) Schematic of the proton transfer reaction observed

final products $CH_2NO_2^-$ and $CH_3NO(OH)^+$. The H transfer event occurs on a time scale of about 15 fs.

Since the C—N bond is the weakest covalent bond in nitromethane, one might think that the C—N bond should break as is commonly observed in the collision simulations of the previous sections. Indeed, Fig. 2.8 reveals that as the compression of the liquid is increased, there is a significant compression of the C—N bond, as compared to the CH and CO bonds. So one question to ask is why then does the C—H bond first break? To answer this question, we used molecular orbital theory and examined the electronic structure of nitromethane. As previously mentioned, it is notable that there is a significant compression of the CN bond as the pressure is increased. Examination of the frontier molecular orbitals of the nitromethane molecule as the C—N bond is shortened reveals that the methyl group proton of nitromethane becomes a

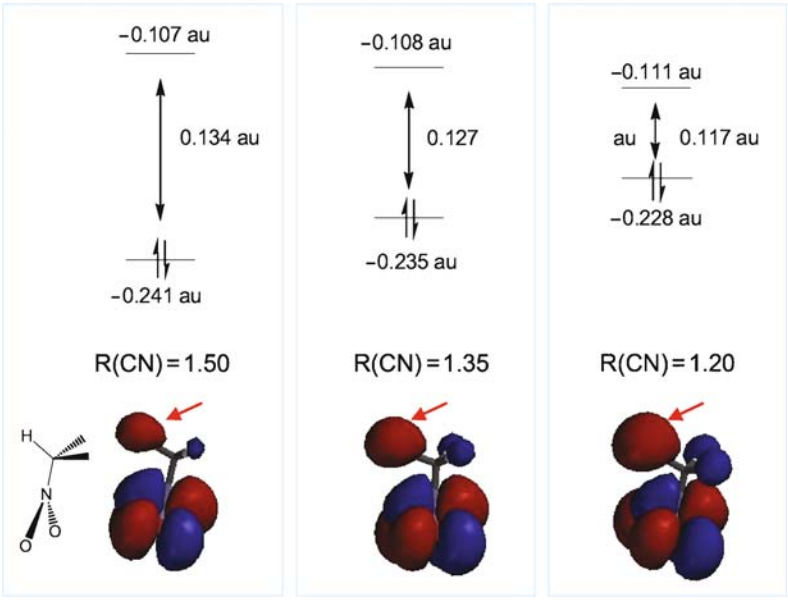

Fig. 2.10. Frontier molecular orbitals of nitromethane as a function of the CN bond length. The top portion of the figure show the calculated orbital energies of the highest occupied molecular orbital (HOMO) and the lowest unoccupied molecular orbital (LUMO). The bottom portion of the figure shows isosurface plots of the LUMO orbital of nitromethane. As the CN bond is compressed the LUMO orbital energy is stabilized, and the orbital lobe on one of the hydrogen atoms becomes larger, as highlighted by the red arrow

better Lewis acid. At the same time, the carbonyl oxygen becomes a better Lewis base. This is illustrated in Fig. 2.10 which shows the highest occupied molecular orbital (HOMO) and lowest unoccupied molecular orbital (LUMO) energies as a function of the C—N bond distance. The HOMO orbital of nitromethane (not shown) can be described as a pi-bonding orbital of the aromatic ONO fragment of nitromethane. This orbital is also polarized toward the oxygen, and as the C—N bond is compressed, it increases in energy, thereby making the oxygen atoms better Lewis base sites. The LUMO of nitromethane, shown on the bottom of Fig. 2.10, can be described as an anti-bonding orbital of the aromatic ONO fragment. However, there is a significant component of this molecular orbital localized on the hydrogen atoms as highlighted by the red arrow in Fig. 2.10. Moreover, this contribution becomes larger and the LUMO energy becomes stabilized as the CN bond is compressed. Both of these show that the nitromethane protons become more Lewis acidic as the CN bond is compressed.

From first principles molecular dynamics simulations, Manaa et al. [59] have also observed proton transfer as the first stage of the nitromethane decomposition reaction at high temperature (3,000 K) and high density

($\rho = 1.97\,\mathrm{g\ cm^{-3}}$) conditions. The same observation was made under shock compression conditions with the shock speed of $7\,\mathrm{km\ s^{-1}}$ [60]. Some early, static high pressure experiments [61] show that the thermal detonation time for deuterated nitromethane is ten times longer than that of ordinary nitromethane. While more recent experiments comparing the detonation of nitromethane and deuterated nitromethane show less dramatic differences [56, 62], the measured particle velocities in the reaction zone of detonation reveal that changes upon deuteration are most distinct in the early part of the reaction zone. Consistent with these experimental results, our calculations do suggest that proton transfer might be important in the initial stages of the reaction. Moreover, the quantum chemical analysis of the proton transfer step as a function of the CN bond distance provides fundamental insight into why this process occurs more readily as the pressure is increased.

2.4 High Pressure Non-molecular Solid Phases of Polynitrogen

A covalent, single-bonded nitrogen phase, analogous to carbon in diamond, has long been thought to exist at high pressures. If such a material were metastable at ambient pressures, it would make an extremely powerful high-energy-density material (HEDM). Due to the uniquely large difference in energy between the N—N single and triple bonds, the energy density of single bonded polymeric nitrogen has been calculated [63] to be at least $0.4\,\mathrm{eV\ cm^{-3}}$, which is about three times that of the most powerful energetic materials known today.

The structure of single-bonded polymeric nitrogen was at first suggested to be that of the known single-bonded forms of nitrogen's group 15 congeners, namely, the black phosphorus (BP) structure and the $A7$ structure of arsenic. In 1992, based on possessing gauche interactions among the lone pairs of adjacent nitrogen atoms, Mailhiot, Yang and McMahan [64] predicted a unique single-bonded structure that has no analogue in other natural structures that they called the *cubic gauche* (CG) structure. Based on first principles calculations, within a large range of atomic volumes, the CG structure was predicted to be more stable than the BP and $A7$ phases. Further computational studies [65] showed that CG might be metastable at ambient pressures, thereby furthering the prospect of using polymeric nitrogen as a practical HEDM.

Experimentally, extensive efforts were made to produce polymeric nitrogen and evidence for non-molecular amorphous phases of nitrogen at 100 GPa and 1,000 K were reported [66–68]. In one such study [66], the amorphous material was even recovered at ambient pressures and low temperature. It is likely that the amorphous materials observed were mixtures of small clusters of non-molecular phases. In 2004, Erements and coworkers reported [69] the synthesis of a crystalline form of single-bonded polymeric nitrogen at pressures

greater than 110 GPa and 2,000 K temperatures. Under these conditions, the molecular nitrogen is transformed into the *cubic gauche* crystal phase. The apparent high energy barrier between molecular and non-molecular phases was overcome by the high temperature synthesis. A strong pressure-dependent hysteresis was observed during the synthesis [66, 69]. The high sensitivity of the final phase on its pre-history was also noted in first-principles simulations [64, 70–72], and suggests the existence of many competing metastable high pressure phases separated by large energy barriers.

Recently, a number of new phases of polymeric nitrogen have been found by first principles molecular dynamics calculations at high pressures and temperatures [70–72]. Alemany and Martins [71] found a metastable metallic phase composed of zig-zag chains of nitrogen atoms packed in a body-centered orthorhombic structure. Through similar MD simulations using temperatures (up to 10,000 K), Martin and coworkers [70] also discovered a metastable non-molecular phase composed of zig-zag chains of alternating N—N single and double bonds. Although not single-bonded, this new zig-zag chain phase is lower in energy than *CG* at low pressures and competitive with *CG* at higher pressures.

2.4.1 Polynitrogen Phases from Simple Cubic Motifs

Although successful, the search for new phases by first principles MD simulations is *ad hoc* in nature and can be very computationally demanding. A systematic method to finding new polymeric nitrogen phases is obviously desirable. The fact that all single-bonded metastable phases of group 15 elements predicted or found in nature can be considered Peierls-like distortions [73] of the simple cubic (*SC*) structure hints at such a method. We have recently developed a systematic method of looking for new structures of solid, single-bonded polymeric nitrogen [74]. The method is a synthesis of modern first principles calculations with the geometrical model of crystal structure developed by Wells [75–77] and Burdett and McLarnan [78]. The procedure effectively exploits the connection of the other structures to the *SC* reference structure, allowing focus on the most physically meaningful structure candidates. The procedure is able to recover all the threefold connected nitrogen allotropes found before, (e.g., *A7, BP, CG*) and eight new metastable single-bonded allotropes.

The approach presented here is based on Peierls-like distortions of the *SC* reference structure in order to systematically generate new single-bonded polynitrogen structures consistent with a threefold connectivity pattern of nitrogen. In the undistorted *SC* structure, each nitrogen atom has six equidistant nearest neighbors. The distortion must be such that each nitrogen atom forms only three covalent bonds, thereby breaking the remaining three of the 'bonds' of the original *SC* structure. To obtain a complete set of possible *SC* distortions consistent with threefold connectivity we use the combinatorial analysis procedure of Burdett and McLarnan [78], which is based on a

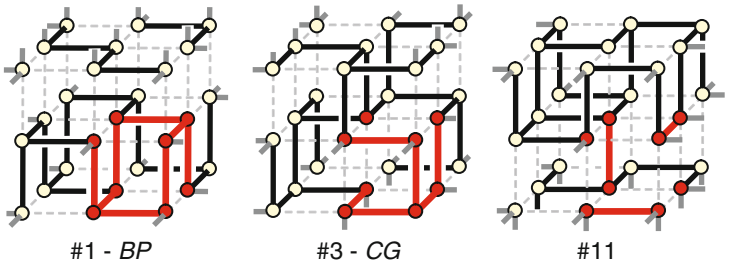

Fig. 2.11. Connectivity diagrams (or structure types) of a simple cubic reference structure consistent with a threefold coordination of nitrogen. Shown are the connectivity diagrams of structure #1, #3 and #11 of a possible 36. The structure numbering that is adopted is that of [78]. A single eight atom SC unit cell is highlighted with red atoms and bonds

generalization of Polya's enumeration theorem [79, 80]. In particular, Burdett and McLarnan show that out of 4,096 possible combinations there are only 36 unique ways of labeling the edges of an eight atom *SC* unit cell as "bonds" and "non-bonds" consistent with the threefold connectivity. Those bond-breaking patterns can be described by connectivity diagrams or structure types, as depicted in Fig. 2.11. The complete specification of all the 36 structure types is provided in [78] and we adhere to the same numbering. Note that all the previously reported structures of single-bonded nitrogen, such as *CG, BP, A7*, and *LB* [72] are covered in the set of 36 structure types. Figure 2.11 shows the connectivity diagrams for *BP* (structure #1), *CG* (#3) and a new structure #11 that will be discussed in further detail later.

Once a structure type is chosen, the next step is to use the connectivity pattern to distort the *SC* structure to generate an initial geometry that can be optimized by first principles calculations. The most straightforward distortion is to displace each atom of the unit cell by a distance, d, along the body diagonal toward the three connected neighbors as shown in Fig. 2.12. Once all atoms are distorted in this way, a rough initial structure is generated as depicted on the r.h.s. of Fig. 2.12. This can be described as a Peierls-like distortion of the *SC* structure. This initial structure acts as a starting point for a series of first principles calculations. In our calculations, we utilized the Kohn–Sham density functional theory calculations with the Perdew–Burke–Ernzerhof (PBE) [27] exchange-correlation functional. The Vienna ab initio simulation package (VASP) [81] was used with the projector augmented wave (PAW) method of Blöchl [82] to treat the core states. A plane-wave cutoff of 39 Ry was used and Brillouin-zone integration was performed using a $8 \times 8 \times 8$ Monkhorst–Pack gamma point centered grid.

Although the generation of the initial structures may seem straightforward, the structures may not be stable at all pressures, if at all. Thus, a careful structure optimization procedure is needed in order to find the appropriate

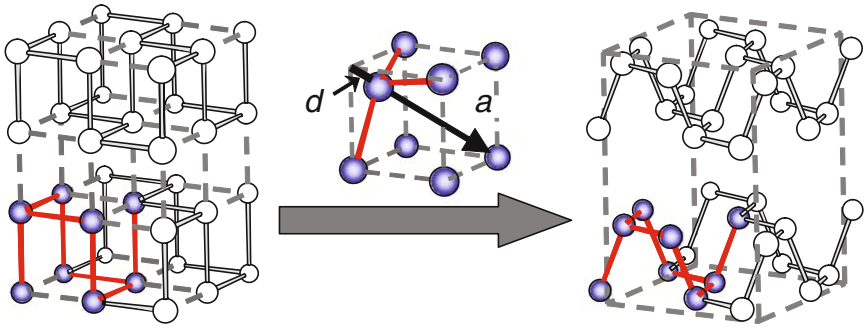

Fig. 2.12. Schematic illustration of the procedure. Left: a structure type of an eight atom cube is first chosen (blue atoms with red bonds). A Peierls-like distortion that is consistent with the connectivity is applied. Right: the structure after distortion of all atoms in an extended representation

ranges of pressure/volume conditions, as well as to prevent premature decomposition of structures before they get sufficiently close to the final optimized geometries.

Here we adopted the following computational procedure. Beginning with the initial structure generated by the aforementioned Peierls-like distortion, the lattice constant a is scanned from 4.1 Å downwards, with a step of 0.05 Å. For each value of a, the following optimization steps are performed.

- First the distortion parameter d is adjusted to minimize the ab initio calculated total energy.
- Then the unit cell shape is allowed to relax, fixing the fractional coordinates of the atoms and the unit cell volume.
- Finally, full relaxation of both the unit cell shape and the atomic positions at fixed unit cell volume a^3 are performed.

At each such relaxation stage the structure must still preserve the intended connectivity pattern. The scan of the lattice constant continues until either the first time a fully optimized structure with a required connectivity pattern is encountered or $a = 3.0$ Å is reached. In cases where a fully optimized structure that preserves the intended structure type is obtained, which happened for 26 out of 36 types, mechanical stability of the structure is verified by calculating the Phonon spectrum, and also the enthalpy-pressure curve. The mechanical stability is inferred from phonon densities of states for each of the 26 structures at various pressures. The stabilities are deduced from a force constant matrix calculated in a $2 \times 2 \times 2$ (64 atom) supercell by means of consecutive displacements of each atom of the original unit cell by 0.02 Å along each axis. In some cases this supercell size may be inadequate, giving rise to false negative frequencies. In this respect, only the affirmative outcomes of the metastability tests should be treated as conclusive.

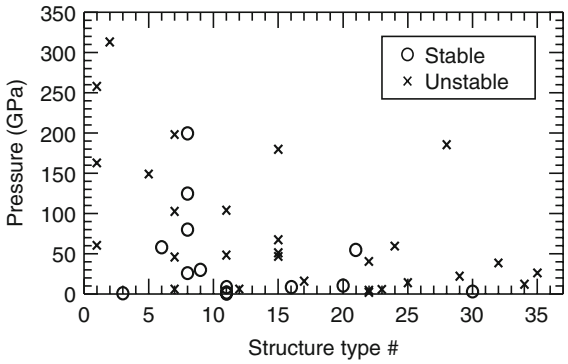

Fig. 2.13. Results of the phonon-spectra based mechanical stability tests for the 36 structure types and different pressures. Mechanically stable and unstable structures at different pressures are shown with circles and crosses, respectively [74]

Analysis of the mechanical stability, shows that at least 8 of the 26 new structures are mechanically stable at pressures less than 100 GPa (#6, 8, 9, 11, 16, 20, 21 and 30). Structures #11 and #30 are even found to be mechanically stable at zero-pressure. The tests of mechanical stability at various pressures are summarized in Fig. 2.13. Figure 2.14 reveals that the *cubic gauche* phase is still the lowest enthalpy structure over the whole pressure range studied. Moreover, it also shows pronounced mechanical stability in our phonon calculations, which is consistent with the same type of analysis in [65]. Leaving the *cubic gauche* case aside, the data in Fig. 2.13 suggest that new structures generated by Peierls distortions, such as structure types #8 and #11, have energies that are comparable or lower than those of the previously studied structures #1 (*BP*), #7 (*AT*), and #15 (*LB*). The 3-dimensional structures of structures #8 and #11 are depicted in Fig. 2.15.

To get an insight into the relative energy rankings of different structure types we analyze a correlation between the first-principles total energies and the number of *cis*-, *gauche*-, *trans*- dihedral angles, and four-member rings of those structure types. Based on such analysis, the lowest energy structures of the low pressure region, structures #3 (*CG*) and #11 (new) are recognized as structures that minimize the number of *trans*-dihedrals and four-member rings while maximizing the *gauche*-dihedrals. It is interesting to note that the stronger weight of *trans*- than the *cis*-dihedrals is in contrast with the simplified "lone-pair" orbital picture [64,78] gained from ab-initio calculations on small nitrogen molecules.

After mechanical stability screening, newly found structures #11 and #8 are the second lowest enthalpy structures after *cubic gauche* at low (<40 GPa) and moderate/high (∼>40 GPa) pressures, respectively. Selected views of structures #11 and #8 are shown in Fig. 2.16. Structure #11 is distinguished by the high R_{32} symmetry and its structure can be described by sets of

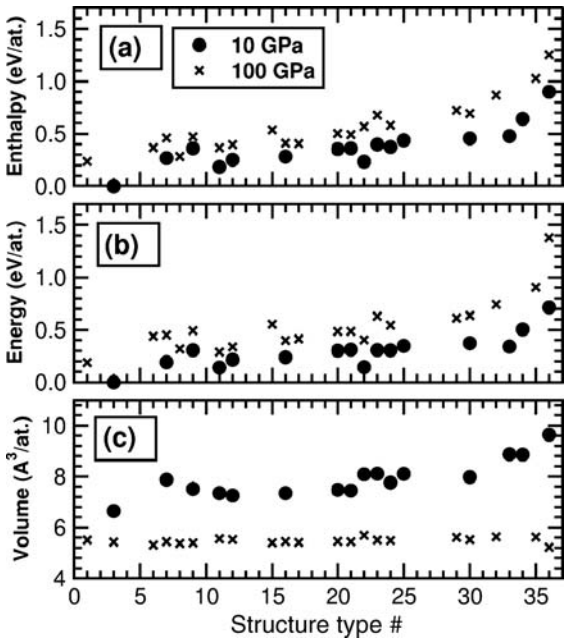

Fig. 2.14. Calculated (**a**) enthalpy, (**b**) total energy, and (**c**) volume per atom versus structure type # at pressures of 10 GPa (circles) and 100 GPa (crosses). The enthalpies and energies are with respect to those of the *CG* phase at the corresponding pressures. Note that structures #1, 3, 7, and 15 are the previously known phases – *BP, CG, A7*, and *LB*, respectively [74]

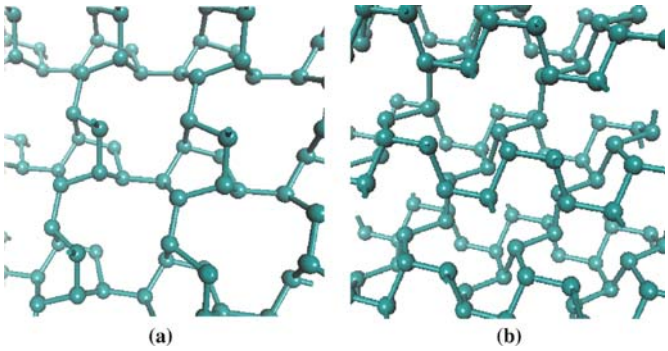

Fig. 2.15. Extended structures of two new low energy and metastable phases, (**a**) structure #11 and (**b**) structure #8

cis–trans chains directed along the three coordinate axes. In fact there are two mutually orthogonal sets of *cis–trans* chains along each axis. Structure #8 has P_{-1} symmetry and a very strong structural resemblance to structure #11, being similarly shaped by sets of *cis–trans* chains but along two out of

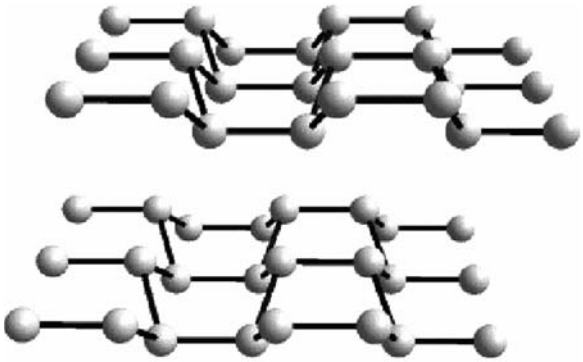

Fig. 2.16. A perspective view of the lattice structure of the Layered-Boat (*LB*) structure

the three axes, hence its lower symmetry. Structure #8 contains large voids in between those layers which may be responsible for the less favorable enthalpy at lower pressure. Structure #11 is an insulator with an indirect band gap decreasing from 2.8 eV at near zero pressure to 2.2 eV at 43 GPa. Structure #8 is also an insulator with an indirect gap at low pressures (e.g., 1.0 eV at 26 GPa) replaced by a higher energy direct gap at higher pressures (1.5 eV at 96 GPa).

2.4.2 Polynitrogen Phases from Chain Motifs

Using a series of high temperature and high pressure ab initio molecular dynamics simulations we have previously found [72] a new single bonded nonmolecular phase that we have named the 'layered boat' or *LB* phase as shown in Fig. 2.16. The new phase consists of layers of fused six-membered rings in a boat conformation, and thus the layered boat name. *LB* has a $P2_1/m$ symmetry and consists of two-dimensional layers of fused N_6-rings where the rings are all in the boat conformation. A calculated enthalpy versus pressure phase diagram reveals that *LB* lies between *BP* and *A7* in enthalpy at pressures less than 200 GPa. At pressures higher than this, the enthalpy of *LB* edges above that of *A7*.

The structure of *LB*, initially obtained at high pressures, remains qualitatively unchanged when re-optimized at different pressures in the range of 0–300 GPa, indicating that, along with other polymeric phases of nitrogen, *LB* is also metastable for a wide range of pressures. An enthalpy versus pressure phase diagram for *LB* and various other phases is shown on Fig. 2.17 for pressures less than 200 GPa. At low pressures, from 0 GPA to 50 GPa, *zzCH* is predicted to be the lowest in enthalpy, in agreement with the work of Mattson et al. [70]. At pressures greater than 50 GPa and less than 200 GPa, *CG* becomes the lowest in enthalpy, and *BP* becomes lowest at even higher pressures. The new phase, *LB*, is higher in enthalpy than *CG* and *zzCH* for all observed pressures and is between *A7* and *BP* for pressures up to 210 GPa.

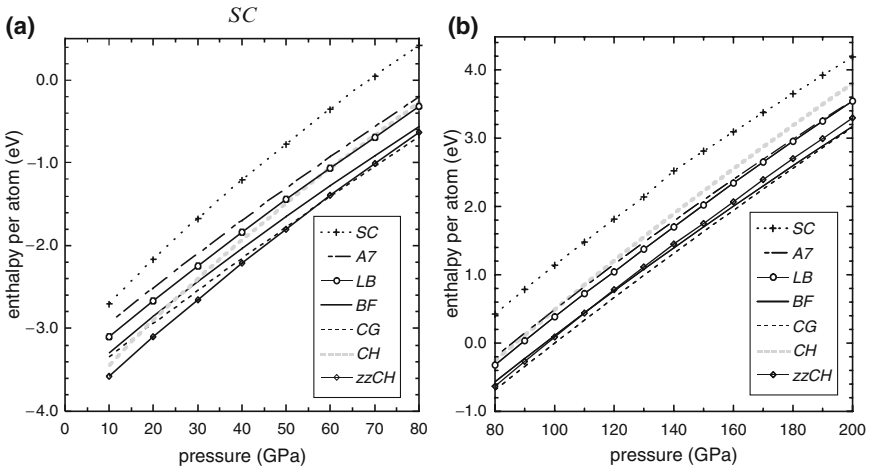

Fig. 2.17. Phase diagram of various polymeric nitrogen phases. The enthalpy per atom is relative to the enthalpy per atom of *CG* at 100 GPa. For clarity, the phase diagram is split into two pressure regions: (**a**) 0–80 GPa and (**b**) 80–200 GPa [72]

At pressures above 210 GPa, *LB* becomes slightly higher in enthalpy than *A7*. *SC* is the least favorable phase among all the phases discussed here. *CH* has the fastest growth of enthalpy with respect to the increasing pressure, and quickly becomes less favorable than all except *SC* as the pressure is increased.

The *LB* phase can be constructed using the *SC* starting structures as described in the previous section. Viewed from an alternative perspective, the structure of the *LB* phase is related to the *BP* and *A7* phases in that they are also composed of layers of fused six-member rings, however, in the latter two the rings are in the chair conformation. The *LB, BP* and *A7* phases can be thought of as different arrangements of the zig-zag chains in the *zzCH* phase approaching along given directions and forming new inter-chain bonds. This is shown in Fig. 2.18 where the *zzCH* phase is depicted with possible inter-chain bonds that would result in the formation of the *LB, BP* and *A7* phases. The two-dimensional layers emerge with a periodic six-ring pattern as a result of the chains in *zzCH* coming close together and forming bonds which change the coordination of the nitrogen atoms from two to three.

In this representation, the 'chains' of *A7* are aligned parallel to each other, and all are simultaneously tilted to one side. In Fig. 2.18 the chains are depicted tilted to the left. An enantiomeric 'right tilted' form of *A7* could be constructed from *zzCH* by choosing a different direction along which the zig-zag chains come together. In the same spirit, *LB* could be characterized as an arrangement of zig-zag chains tilted to the left and right in an alternating fashion. The relationship between the layered phases and the *zzCH* phase outlined here is not meant to show how the layered phases are most favorably formed from the *zzCH* phase. Nonetheless, it provides possible pathways

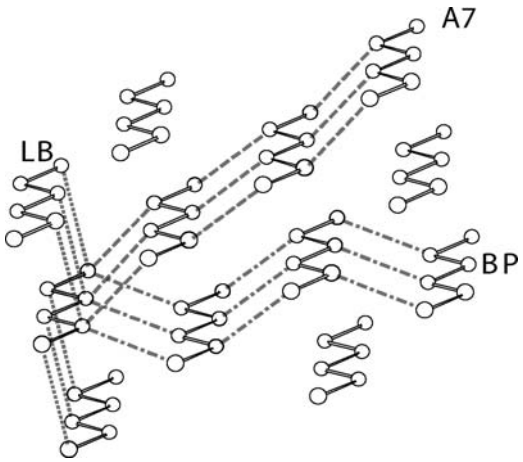

Fig. 2.18. The *zzCH* phase with the possible inter-chain bonding drawn: *BP* (*dash-dot lines*), *A7* (*dash lines*) and *LB* (*dot lines*)

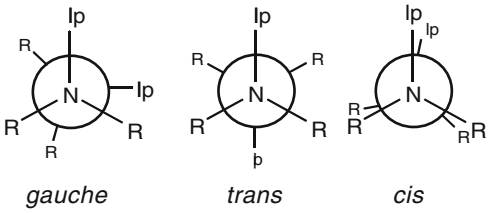

Fig. 2.19. Newman projections of the $R_2N—NR_2$ fragment in various conformations. 'lp' represents the lone-pair

for the formation of the layered phases from the *zzCH* phase that do not require significant structural rearrangement. We note that both *BP* and *LB* can also be considered in terms of *cis–trans* chains of the *CH* phase coming close together and forming inter-chain bonds.

The three layered phases, *A7, BP*, and *LB* all consist of fused six-member rings composed of nitrogen atoms that are sp^3 hybridized. The local structure of the three phases is distinct, for example, the rings in *A7* and *BP* are in the chair conformation whereas they are in the higher energy boat conformation in *LB*. Here we examine the relationship between the local structure and the relative internal energies of the phases by considering the dihedral angles between N—N single bonds.

Quantum chemical calculations of small molecules of the form $R_2N—NR_2$ (R = H, CH_3, etc) show that they have two minimum energy conformers – *gauche* and *trans* as depicted in Fig. 2.19. The *gauche* structure of $R_2N—NR_2$ is not ideal in that the lp—N—N—lp dihedral angle, θ, is not 60° but 90°. The 90° dihedral angle of the *gauche* conformer can be accounted for by the fact that this θ angle minimizes the two-orbital/four-electron destabilizing

interaction between the two lone pair orbitals of the adjacent N atoms. (We note that gauche definition sometimes used is somewhat different than the convention used here. For example, the lp—N—N—lp dihedral angle, in the *cubic gauche* phase is 107° with a lp—N—N—R dihedral angle being close to zero.) For a later discussion we also introduce the *cis* conformation where the lp—N—N—lp = 0°. This is actually the maximum energy conformation as the lp—N—N—lp is rotated through 360°.

The energy of the N—N moiety depends on the mutual orientation of two adjacent lone-pairs as defined by the lp—N—N—lp dihedral angle. The structure of *CG* was postulated [64] as a solid phase of nitrogen that has all of its single bonds in a gauche dihedral conformation. Indeed, our calculations as well as many others [64, 70, 71, 83] demonstrate that above 50 GP, *CG* has the lowest enthalpy among all the known nitrogen phases.

The internal energy of the *A7, BP*, and *LB* phases can be related to the ratio of *gauche, trans* and *cis* N—N bonds there are in each phase. There are six such dihedral angles in each six-member ring of these phases. *BP* has a ratio of 4-*gauche*/2-*trans*/0-*cis*, while *A7* has a ratio of 0-*gauche*/6-*trans*/0-*cis* and *LB* has a ratio 0-*gauche*/4-*trans*/2-*cis*. With the *gauche* conformation being the most stable, followed by the *trans*-conformation and the *cis* conformation being the least stable, it is clear that this simple structural analysis predicts the following ordering of the three layered six-member ring phases: $BP < A7 < LB$. First-principles computations of the three phases are in agreement with this. The calculated internal energy per atom of the phases is $-268.6710\,\text{eV} < -268.6103\,\text{eV} < -268.5912\,\text{eV}$ at 20 GPa. Of course, the overall enthalpy of the phases contains a volume factor, which has substantial contribution at elevated pressures.

2.4.3 Polynitrogen Phases from Helical Motifs

Helical chains can also be considered as a natural structural theme in polymeric nitrogen phases. Recognition of helical structural motifs in the experimentally observed *CG* crystal lattice has lead to the discovery of a new single-bonded non-layered nitrogen structure named *chaired web* (*CW*) [84]. First-principles density functional theory calculations reveal that *CW*, which was originally identified at high pressures is metastable at ambient conditions as well. The metastability is demonstrated by both high-quality phonon dispersion calculations and finite temperature first-principles molecular dynamics simulations. In addition the new *CW* phase is thermodynamically more stable than the *CG* phase in the ambient pressure regime.

The results were obtained by first principles density functional theory calculations with the Perdew–Burke–Ernzerhof (PBE) [27] exchange-correlation functional. The SIESTA [85] package was used for most of the exploratory simulations, preliminary optimization of structures, and molecular dynamics simulations, while VASP [81] was used to calculate the final phase diagram, phonon dispersion and band structure. For the SIESTA calculations,

the Troullier–Martins [86] norm-conserving pseudopotential with a nitrogen reference configuration of $[He]2s^2 2p^3$ and a cut-off radius of 0.98 Å was utilized. A custom numerical 'double-zeta with polarization' SIESTA-type basis set [87] was developed for the calculations. A 10 Å cut-off was employed for the k-point sampling. The calculations performed with VASP were based on the projector augmented wave (PAW) method of Blöchl [82] where a 39 Ry plane wave cutoff and Brillouin-zone integration with $12 \times 12 \times 12$ Monkhorst–Pack grid were used. In both programs a variable-cell-shape conjugate gradient method under constant pressure was used for the minimization of the geometries, and molecular dynamics was performed within the Nosé–Parinello–Raman scheme.

Ab-initio calculations on small Molecules of the type R_2—N—N—R_2 demonstrated that the most favorable dihedral angle is the so-called *gauche* dihedral, i.e., ∼120°, due to the effect of hyperconjugation and mutual repulsion of nitrogen lone electron pairs [64]. A chain of atoms constructed with all *gauche* dihedral angles results in the formation of right- or left-handed helices, depending on whether a dihedral of +120° or −120° is applied. Indeed, within the *CG* structure, helices that have four and eight atoms per turn can be identified along the [100] direction and threefold helices can be located along the [110] direction. Figure 2.20d highlights the eightfold helices in *CG*.

Pure helices are also observed in some high pressure phases of group 16 elements, such as sulfur, selenium and tellurium [88–90] as well as in scandium [91]. Unlike the group 16 elements, nitrogen cannot form stable helices on its own. In order to acquire stability a single helical chain of nitrogen atoms has to have its valence saturated (form three single bonds). If the valence is not saturated, then partial double bonds will form and the chain will flatten out to either a *cis–trans* or zig-zag chain. In the latter case the

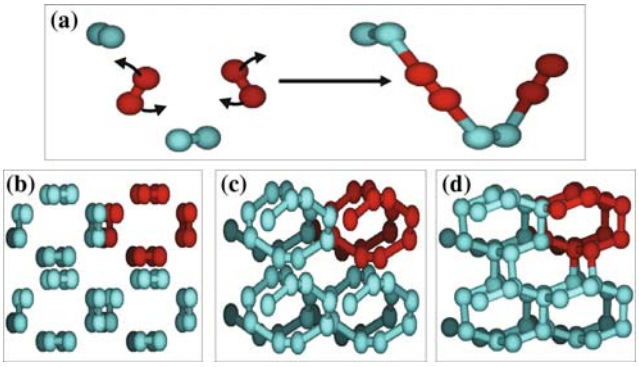

Fig. 2.20. (**a**) Flipping or 'inverting' two (highlighted in red) out of four N_2 molecules in the primitive unit cell of the molecular ζ-phase (l.h.s.) results in an eightfold helical chain structure (r.h.s.) (**b**) ζ-phase, (**c**) 'inverted' ζ-phase and (**d**) *CG*. For B, C and D a $2 \times 2 \times 2$ supercell is shown with one helical chain highlighted in red [84]

energy lowers by 0.5 eV per atom. The reverse tendency also holds, namely *cis–trans* or zig-zag chains acquire helicity once capped due to the above mentioned 'gauche-effect' and the energy is lowered by 0.6 eV per capped atom. It is interesting to note that in both cases the lowering of energy is achieved by changes in the local hybridization (from sp^3 to sp^2 and vice versa), symmetry breaking and splitting of degeneracy at the Fermi level. These are characteristic of a Peierls deformation. If a pure nitrogen structure is sought, the helices have to be brought close enough to each in order to create inter-helical bonds. The geometry of *CG* could be thought of as such a structure where interlinked nitrogen helices form a single-bonded network as illustrated in Fig. 2.20d.

The base helical structure of *CG* can be formed from what has been proposed to be the molecular ζ-phase, which itself is considered to be the immediate molecular precursor [92] of *CG* during its synthesis. Helices can be formed by changing the alignment of two out of the four N_2 molecules within the primitive unit cell of the ζ-structure. The necessary rotation about the two molecule's center of mass as to 'invert' their orientation is shown in Fig. 2.20a. Using this 'inverted' ζ-structure (Fig. 2.20b) as a starting geometry for a first-principles calculation, eightfold helical chains form after only a few optimization steps as depicted in Fig. 2.20c. Further optimization at high pressure leads to the formation of the single-bonded *CG* phase (Fig. 2.20d). In a similar manner the geometry optimization of properly arranged four- and threefold helical chains also result in the formation of *CG*.

It is natural to propose that certain arrangements of the helical nitrogen chains could form the basis of other polynitrogen structures. To achieve a structure where all nitrogen atoms are three-coordinate, bonds between adjacent chains must be made because the nitrogen atoms are only two-coordinate in the pure helical chains. Different arrangements of 3-, 4-, *etc.* fold helices or of their combinations could lead to alternative structures. For example, a slight rearrangement of the threefold helices within *CG* results in a structure that has recently been proposed as a new polynitrogen structure [93]. Arrangement and connection of sixfold helical chains as shown in Fig. 2.21, followed by geometry optimization, produced a new stable structure we have called *chaired-web* (*CW*). Connecting the helical chains together, results in the

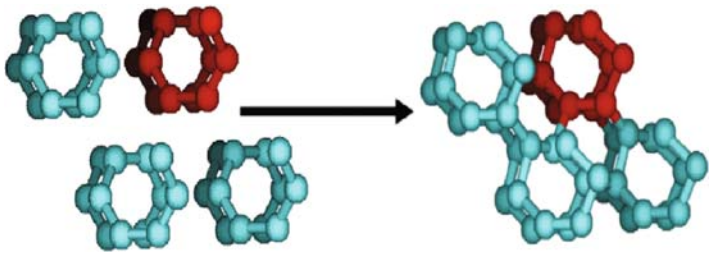

Fig. 2.21. A properly arranged set of sixfold helices (l.h.s.) forming the single-bonded *CW* phase (r.h.s) [84]

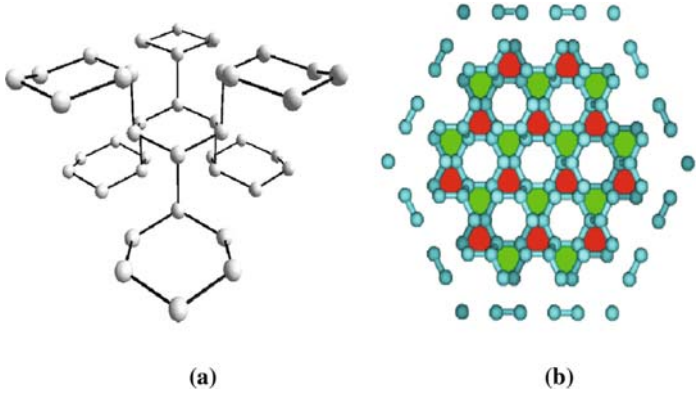

Fig. 2.22. Lattice structure of *CW*: (**a**) Perspective view, (**b**) A view along [111]. Left- (red) and right- (green) oriented sixfold helices with six-rings (white) lying between them within *CW* phase ($3 \times 3 \times 3$ supercell) [84]

formation of a network of six-member rings that are in the so-called 'chair' conformation, as the name given to the structure suggests. Figure 2.21a highlights the six-member rings of the *CW*.

The structure and symmetry of the new phase is better seen in Fig. 2.22. If the original helices turn clockwise (depicted in Fig. 2.22b in red) then new helices with counter-clockwise turns (depicted in Fig. 2.22b in green) are naturally formed in between the original helices due to the inter-helical bonds. The aforementioned six-member rings are formed in the voids between the helices as shown in white in Fig. 2.22b. These voids accommodate the nitrogen lone pairs. All of the six-member rings are in the so-called chair conformation. The interplay of helical chain and six-ring structural motifs in *CW* is reminiscent of *cis–trans* chain and six-member ring motifs interplay in the layered phases *BP, A7* and *LB* discussed above [72]. Additionally, we note that the structure of *CW* can be obtained by applying the Peierls distortion method for generating purely single-bonded polymeric nitrogen [74]. However, the 8-atom simple cubic reference cell first demonstrated [74] would not be large enough to generate *CW*. Rather a significantly expanded 48 atom (or larger) simple cubic reference structure would have to be employed.

The primitive unit cell of *CW* is rhombohedral. At an intermediate pressure of 28 GPa the unit cell vector length is 3.5 Å with an angle measuring 99.172° and the corresponding symmetry group is R $\bar{3}$m. The six equivalent atomic positions obtained by the use of symmetry in fraction coordinates are (0.8756, 0.8756, 0.3206). There are two types of interatomic distances in the crystal lattice, a shorter N—N distance within a given six-member ring and slightly longer N—N distance between two adjacent six-member rings. At 28 GPa these distances are 1.36 Å and 1.45 Å respectively. There is a 2:1:0 ratio of *gauche-*, *trans-* and *cis-* dihedral angles in the crystal lattice. Band structure

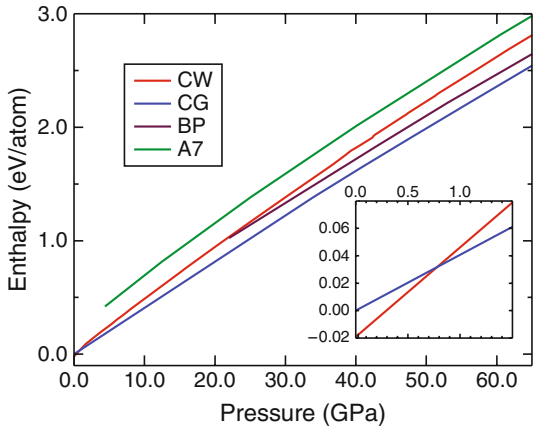

Fig. 2.23. Relative enthalpy versus pressure phase diagram of *CW, CG, BP* and *A7*. Enthalpy is relative to CG at 0° pressure. The inset in the lower right corner enlarges the low-pressure region [84]

calculations show that *CW* is an insulator at low pressure with a calculated band gap of ~ 5 eV. The phase diagram shown on Fig. 2.23. demonstrates how close *CW* is to *CG* in terms of enthalpy. At zero pressure the enthalpy favors *CW* over *CG* by approximately 20 meV. The temperature-dependant free-energy and zero-point energy corrections within the harmonic approximation have been evaluated at zero pressure. The zero-point energy correction favors *CG* over *CW* by 54 meV thus reversing the energy order of the two phases at zero temperature. With the raise in temperature there is a cross-over of the two free-energy dependencies around 200 K. At ambient temperature the new *CW* phase is thermodynamically more stable than the *CG* phase with 83 meV in free energy.

The results of high-quality phonon dispersion calculations reveals that the *CW* phase is metastable at very low pressures. Although the lack of negative frequencies in the phonon dispersion calculation is theoretically rigorous verification of *CW*'s metastability (at least at low temperatures), three additional tests to probe the energy barrier of decomposition have also been performed: (i) a random displacement test in which the structure is optimized after the positions of atoms are randomly displaced by 5% of their inter-atomic distance; (ii) ab-initio molecular dynamics test at 0 GPa, 300 K for 10 ps. (iii) a hybrid test in which ten random snapshots of the initially equilibrated system are taken, the positions and velocities are randomly perturbed, and the system is further a subject to AIMD at 0 GPa, 300 K for an additional 4 ps. A rigorous study of *CW*'s metastability lifetime is substantially more challenging, but the tests indicate that the lifetime of *CW* may be of practical interest.

The structure of *CW* is, as are other purely single-bonded polymeric nitrogen phases, governed to a large extent by the repulsion of the lone pairs.

In *CW* the inherent stability of the initial *gauche* helices and the newly formed helices of reverse handedness, is offset by the repulsion of the lone pairs from neighboring helices. Importantly, in *CW* the lone pairs point into large void spaces, thereby reducing the repulsion. At high pressure the large voids are thermodynamically unfavorable because of the associated enthalpic penalty. On the other hand, at low pressure, the balance between these two contradictory influences of the lone pairs is such that *CW* is more stable than *CG* at ambient pressures.

In looking for a possible precursor of *CW* one has to note that the traditional understanding of N_2 phase diagram was recently questioned and preliminary results suggest the need for its extension and/or revision [94]. In particular, Gregoryanz et al. [95] found a molecular phase characterized by a configuration of three nitrogen molecules nearly forming a six-member ring. One could speculate that *CW* could be formed from such a phase under appropriately engineered physical conditions.

2.5 Final Remarks

The results presented in this chapter indicate that significant progress can be achieved in applying various first-principles computational methods for atomic-scale descriptions of energetic systems in gas, liquid or solid phases. Using well developed computational chemistry methods it has been possible to determine accurate information about the structural properties of various systems, the relative stabilities of different configurations in different phases, and the decomposition reaction mechanisms. These types of data allowed a direct correlation and interpretation of the corresponding experimental data. Moreover, in many instances the type of data obtained theoretically has substituted for the lack of information achievable through experimental means. This is particularly the case for example, for description of complicated reaction mechanisms where accurate identification of transition states for various pathways is experimentally very challenging.

Beside structural and energetic data, important steps have also been achieved computationally in description of the dynamic processes in condensed phases. Among the computational methods used, first principles calculation methods are the first choice to accurately evaluate the structural, energetic, electronic, and even spectral data.

Alternatively, the progress made in computational hardware and in computational algorithms should allow further development of combined quantum mechanical/molecular mechanical methods for description of energetic and dynamical problems, for systems of increased size and complexity. The use of ab initio molecular dynamics methods for description of the properties of ionic systems is another area which is expecting to grow in importance and relevance.

Acknowledgments

The authors would like to thank our coworkers who have contributed to the work presented here: Dr. Dongqing Wei, Dr. Steven Decker, Dr. Federico Zahariev, Dr. Nick Mosey, Dan Chau and James Hooper. The authors are grateful to Defence R&D Canada-Suffield, NSERC of Canada, the Canada Research Chair program, the Canada Foundation for Innovation, Ontario Innovation Trust and SHARCNet of Canada for a financial support.

References

1. Rahman, A.: Phys. Rev. A **136**, 405 (1964)
2. Verlet, L.: Phys. Rev. **1950**, 98 (1967)
3. Car, R., Parrinello, M.: Phys. Rev. Lett. **55**, 2471 (1985)
4. Parrinello, M.: Solid State Commun. **38**, 115 (1997)
5. Tse, J.S.: Annu. Rev. Phys. Chem. **53**, 249 (2002)
6. Dremin, A.N., Klimenko, V.-Y.: In: Bowen, J.R. (ed.) Progress in Astronautics and Aeronautics, pp. 253. AIAA, New York (1981)
7. Brenner, D.W., Robertson, D.H., Elert, M.L., White, C.T.: Phys. Rev. Lett. **70**, 2174 (1993)
8. Haskins, P.J., Cook, M.D., Fellows, J., Wood, A.: In: Proceedings of the 6th Symposium (International) on Detonation Snowmass, p. 897. Colorado (2000)
9. Barrett, J.J.C., Brenner, D.W., Robertson, D.H., White, C.T.: In: Schmidt, S.C., Tao W.C. (eds.) Shock Compression of Condensed Matter – AIP Conference Proceedings 370, pp. 191. American Institute of Physics, New York (1995)
10. Dremin, A.N.: Philos Trans R Soc Lond A **339**, 355 (1992)
11. Koch, W., Holthausen, M.C.: A Chemist's Guide to Density Functional Theory. Wiley-VCH, Weinheim (2001)
12. Abell, G.C.: Phys. Rev. B Condens. Matter Mater Phys. **31**, 6184 (1985)
13. Tersoff, J.: Phys. Rev. Lett. **56**, 632 (1986)
14. Brenner, D.W.: Phys Status Solidi B **217**, 23 (2000)
15. Hohenberg, P., Kohn, W.: Phys. Rev. **136**, B864 (1964)
16. Kohn, W., Sham, L.: J.Phys. Rev. **140**, A1133 (1965)
17. Fermi, E.: Rend. Accad. Lincei **6**, 602 (1927)
18. Thomas, L.H.: Proc. Camb. Phil. Soc. **23**, 542 (1927)
19. Teller, E.: Rev. Mod. Phys. **34**, 627 (1962)
20. Perdew, J.P., Wang, Y.: Phys. Rev. B **45**, 13244 (1992)
21. Vosko, S.J., Wilk, L., Nusair, M.: Can. J. Phys. **58**, 1200 (1980)
22. Adamo, C., di Matteo, A., Barone, V.: Adv. Quantum Chem. **36**, 45 (1999)
23. Ernzerhof, M., Scuseria, G.E.: J. Chem. Phys. **110**, 5029 (1999)
24. Bauschlicher, Jr. C.W.: Chem. Phys. Lett. **246**, 40 (1995)
25. Becke, A.D.: Phys. Rev. A **38**, 3098 (1988)
26. Perdew, J.P.: Phys. Rev. B **33**, 8822 (1986)
27. Perdew, J.P., Burke, K., Ernzerhof, M.: Phys. Rev. Lett. **77**, 3865 (1996)
28. Becke, A.D.: J. Chem. Phys. **98**, 5648 (1993)
29. Becke, A.D.: J. Chem. Phys. **98**, 5612 (1993)
30. Curtiss, L.A., Raghavachari, K., Trucks, G.W., Pople, J.A.: J. Chem. Phys. **94**, 17221 (1991)

31. Zhao, Y., Gonzalez-Garcia, N., Truhlar, D.G.: J. Phys. Chem. A **109**, 2012 (2005)
32. Szabo, A., Ostlund, N.S.: Modern Quantum Chemistry: Introduction to Advanced Electronic Structure Theory. McGraw-Hill, New York (1989)
33. Boys, S.F.: Proc. R. Soc. Lond. A **200**, 542 (1950)
34. Ashcroft, N.W., Mermin, N.D.: Solid State Physics. Holt Saunders, Philadelphia, PA (1976)
35. Allen, M.P., Tildesley, D.J.: Computer Simulation of Liquids. Oxford University Press, Oxford (1989)
36. Allen, M.P.: In: Attig, N. et al. (eds.) Computational Soft Matter: From Synthetic Polymers to Proteins, Lecture Notes, pp. 1. John von Neumann Institute for Computing, Jülich (2004)
37. Rapaport, D.C.: The Art of Molecular Dynamics Simulation. Cambridge University Press, Cambridge (2004)
38. Frenkel, D., Smit, B.: Understanding Molecular Simulation: From Algorithms to Applications. Academic Press, San Diego, CA (2002)
39. Marx, D., Hutter, J.: In: Grotendorst J (ed) Modern Methods and Algorithms of Quantum Chemistry, pp. 301. John von Neumann Institute for Computing, Jülich (2000)
40. Mosey, N.J., Muser, M.H., Woo, T.K.: Science **307**, 1612 (2005)
41. Alfè, D., Gillan, M.J., Price, G.D.: Nature **401**, 462 (1999)
42. Cavazzoni, C., Chiarotti, G.L., Scandolo, S., Tosatti, E., Bernasconi, M., Parrinello, M. Science **283**, 44 (1999)
43. Alavi, S., Thompson, D.L.: J. Chem. Phys. **120**, 10231 (2004)
44. Alper, H.E., Abu-Awwad, F., Politzer, P.: J. Phys. Chem. B **103**, 9738 (1999)
45. Liu, H., Zhao, J., Ji, G., Gong, Z., Wei, D.: Physica B **382**, 334 (2006)
46. Riad Manaa, M., Reed, E.J., Fried, L.E., Galli, G., Gygi, F.: J. Chem. Phys. **120**, 10146 (2004)
47. Siavosh-Haghighi, A., Thompson, D.L.: J. Chem. Phys **125**, 184711/1 (2006)
48. Sorescu, D.C., Rice, B.M., Thompson, D.L.: J. Phys. Chem. A **105**, 9336 (2001)
49. Tuckerman, M.E., Klein, M.L.: Chem. Phys. Lett. **283**, 147 (1998)
50. Zheng, L., Luo, S.-N., Thompson, D.L.: J. Chem. Phys. **124**, 154504/1 (2006)
51. Winey, J.M., Gupta, Y.M.: J. Phys. Chem. B, **101**, 10733 (1997)
52. Piermarini, G.J., Block, S., Miller, P.J.: J. Phys. Chem. **93**, 457 (1989)
53. Haskins, P.J., Cook, M.D.: In: Schmidt, Dandekar, Forbes (eds.) Shock Compression of Condensed Matter, p. 305 (1997)
54. Wei, D., Zhang, F., Woo, T.K.: Proceedings of the, Atlanta, GA. In: 12th Biennial International Conference of the APS Topical Group on Shock Compression of Condensed Matter, pp. 407. American Institute of Physics, Atlanta, GA, USA (2001)
55. Graham, R.A.: J. Phys. Chem. **83**, 3048 (1979)
56. Sheffield, S.A., Engelke, R., Alcon, R.R., Gustavsen, R.L., Robbins, D.L., Stal, D.B., Stacy, H.L., Whitehead, M.C.: In: Proceedings of 12th International Detonation Symposium, pp. 159. Office of Navy Research, Arlington, VA, San Diego, CA, USA (2002)
57. Higgins, A.J., Jetté, F.X., Yoshinaka, A., Zhang, F.: In: Proceedings of 12th International Detonation Symposium, pp. 993. Office of Navy Research, Arlington, VA, San Diego, CA, USA (2002)

58. Yoshinaka, A., Zhang, F., Petel, O.E., Higgins, A.J.: In: Proceedings of the Shock Compression of Condensed Matter Conference, pp. 1139. American Institute of Physics, Baltimore, MD (2005)
59. Manaa, M.R., Reed, E.J., Fried, L.E., Galli, G., Gygi, F.: J. Chem. Phys. **120**, 10146 (2004)
60. Manaa, M.R.: Chemistry at Extreme Conditions. Elsevier, Amsterdam (2005)
61. Shaw, R., Decarli, P.S., Ross, D.S., Lee, E.L., Stromberg, H.D.: Combust. Flame **35**, 237 (1979)
62. Sheffield, S.A., Davis, L.L., Engelke, R.: In: Furnish, M.D., Chhabildas, L.C., Hixson, R.S. (eds.) Shock Compression of Condensed Matter, pp. 789. American Institute of Physics, Snowbird, Utah (1999)
63. Uddin, J., Barone, V., Scuseria, G.E.: Mol. Phys. **104**, 745 (2006)
64. Mailhiot, C., Yang, L.H., McMahan, A.K.: Phys. Rev. B **46**, 14419 (1992)
65. Barbee, T.W., III, Phys. Rev. B **48**, 9327 (1993)
66. Eremets, M.I., Hemley, R.J., Mao, H.-k., Gregoryanz, E.: Nature **411**, 170 (2001)
67. Goncharov, A.F., Gregoryanz, E., Mao, H.-k., Liu, Z., Hemley, R.J., Phys. Rev. Lett. **85**, 1262 (2000)
68. Gregoryanz, E., Goncharov, A.F., Hemley, R.J., Mao, H.-k., Somayazulu, M., Shen, G.: Phys. Rev. B **66** (2002)
69. Eremets, M.I., Gavriliuk, A.G., Trojan, I.A., Dzivenko, D.A., Boehler, R.: Nat Mater **3**, 558 (2004)
70. Mattson, W.D., Sanchez-Portal, D., Chiesa, S., Martin, R.M.: Phys. Rev. Lett. **93**, 125501/1 (2004)
71. Alemany, M.M.G., Martins, J.L.: Phys. Rev. B **68**, 024110/1 (2003)
72. Zahariev, F., Hu, A., Hooper, J., Zhang, F., Woo, T.: Phys. Rev. B **72** (2005)
73. Peierls, R.: Quantum Theory of Solids. Pergamon, Oxford (1955)
74. Zahariev, F., Dudiy, S.V., Hooper, J., Zhang, F., Woo, T.K., Phys. Rev. Lett. **97** (2006)
75. Wells, A.F.: Models in Structural Inorganic Chemistry. Clarendon Press, Oxford (1970)
76. Wells, A.F.: Three-dimensional Nets and Polyhedra. Wiley, New York (1977)
77. Adams, D.M.: Inorganic Solids. Wiley, London (1974)
78. Burdett, J.K., McLarnan, T.J.: J. Chem. Phys. **75**, 5764 (1981)
79. Poya, G.: Acta Math. **68**, 145 (1937)
80. Hararay, F.: Graph Theory. Addison-Wesley, Reading, MA (1994)
81. Kresse, G., Furthmuller, J.: Phys. Rev. B **54**, 11169 (1996)
82. Bloechl, P.E.: Phys. Rev. B **47**, 17953 (1994)
83. Nordlund, K., Krasheninnikov, A., Juslin, N., Nord, J., Albe, K.: Europhys. Lett. **65**, 400 (2004)
84. Zahariev, F., Hooper, J., Alavi, S., Zhang, F., Woo, T.K.: Phys. Rev. B **75** (2007)
85. Soler, J.M., Artacho, E., Gale, J.D., Garcia, A., Junquera, J., Ordejon, P., Sanchez-Portal, D.: J. Phys. Cond. Matt. **14**, 2745 (2002)
86. Troullier, N., Martins, J.L.: Phys. Rev. B **45**, 1993 (1997)
87. Junquera, J., Paz, O., Sanchez-Portal, D., Artacho, E.: Phys. Rev. B **64**, 235111 (2001)
88. Hemley, R.J., Mao, H.-k., Struzhkin, V.: J. Synchrotron Rad. **12**, 135 (2005)
89. Crapanzano, L., Crichton, W.A., Monaco, G., Bellissent, R., Mezouar, M.: Nat Mater **4**, 550 (2005)
90. Decker, A., Landrum, G.A., Dronowski, R.: Z. Anorg. Allg. Chem. **628**, 295 (2002)

91. Akahama, Y., Fujihisa, H., Kawamura, H.: Phys. Rev. Lett. **94**, 195503 (2005)
92. Eremets, M.I., Gavriliuk, A.G., Serebryanaya, N.R., Trojan, I.A., Dzivenko, D.A., Boehler, R., Mao, H.-k., Hemley, R.J.: J. Chem. Phys. **121**, 11296 (2004)
93. Oganov, A.R., Glass, C.W.: J. Chem. Phys. **124**, 244704 (2006)
94. Gregoryanz, E., Sanloup, C., Bini, R., Kreutz, J., Jodl, H.J., Somayazulu, M., Mao, H., Hemley R.J.: J. Chem. Phys. **124**, 116102 (2006)
95. Sanloup, C., Gregoryanz, E., Somayazulu, M., Hemley, R.J., Mao, H.K., Goncharov, A.F.: In: Joint 20th AIRAPT – 43rd EHPRG, Karslruhe, Germany, 2005

http://www.springer.com/978-3-540-77078-7

Shock Wave Science and Technology Reference Library,
Vol. 3
Solids II
Horie, Y. (Ed.)
2009, XIII, 280 p. 149 illus., 13 illus. in color., Hardcover
ISBN: 978-3-540-77078-7